

Capsule Formation, Carboxylate Exchange, and DFT Exploration of Cadmium Cluster Metallocavatands: Highly Dynamic Supramolecules

Peter D. Frischmann,[†] Glenn A. Facey,[‡] Phuong Y. Ghi,[‡] Amanda J. Gallant,[†] David L. Bryce,^{*,‡} Francesco Lelj,^{*,§} and Mark J. MacLachlan^{*,†}

Department of Chemistry, University of British Columbia, 2036 Main Mall, Vancouver, British Columbia V6T 1Z1, Canada, Department of Chemistry and Centre for Catalysis Research and Innovation, University of Ottawa, D'Iorio Hall, 10 Marie Curie Pvt., Ottawa, Ontario K1N 6N5, Canada, and La.M.I. and LaSSCAM INSTM Sezione Basilicata, Dipartimento di Chimica, Università della Basilicata, via N. Sauro 85, 85100 Potenza, Italy

Received December 14, 2009; E-mail: mmaclach@chem.ubc.ca; david.bryce@uottawa.ca; francesco.lelj@unibas.it

Abstract: A family of molecular heptacadmium carboxylate clusters templated inside [3 + 3] Schiff base macrocycles has been isolated and studied by variable temperature solution and solid-state NMR spectroscopy, single-crystal X-ray diffraction (SCXRD), and density functional theory (DFT) calculations. These metallocavatand cluster complexes adopt bowl-shaped structures, induced by metal coordination, giving rise to interesting host–guest and supramolecular phenomena. Specifically, dimerization of these metallocavatands yields capsules with vacant coordination and hydrogen-bonding sites accessible to encapsulated guests. Strong host–guest interactions explain the exceptionally high packing coefficient (0.80) observed for encapsulated *N,N*-dimethylformamide (DMF). The guest-accessible hydrogen-bonding sites arise from an unusual μ_3 -OH ligand bridging three cadmium ions. Thermodynamic and kinetic studies show that dimerization is an entropy-driven process with a highly associative mechanism. In DMF the exchange rate of peripheral cluster supporting carboxylate ligands is intrinsically linked to the rate of dimerization and these two seemingly different events have a common rate-determining step. Investigation of guest dynamics with solid-state ²H NMR spectroscopy revealed 3-fold rotation of an encapsulated DMF molecule. These studies provide a solid understanding of the host–guest and dynamic properties of a new family of metallocavatands and may help in designing new supramolecular catalysts and materials.

Introduction

The ability to selectively confine metal clusters to desired size domains helped usher in the age of nanoscience, giving rise to materials with exceptional novelty.¹ Besides numerous materials science applications,² synthesis of molecular metal clusters is paramount in the design of multimetallic catalysts³ and enzyme mimics.⁴ Template-directed or aggregation-based synthetic approaches are most often employed to access complex multimetallic clusters.⁵ For example, both approaches have been used to synthesize models of the Fe₇Mo cofactor in nitrogenase enzymes, a highly sought after complex for elucidating the

mechanism of nitrogen fixation.^{4,6} Metal clusters mimicking enzyme active sites as well as nonbiological systems have proven to be powerful catalysts, allowing or accelerating a

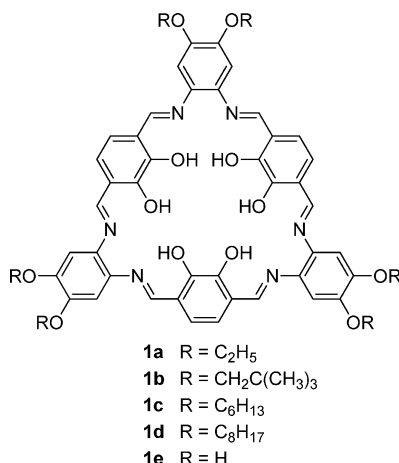
[†] University of British Columbia.

[‡] University of Ottawa.

[§] Università della Basilicata.

- (1) (a) Ozin, G. A.; Arsenault, A. C. *Nanochemistry*; Royal Society of Chemistry: Cambridge, 2005. (b) Ozin, G. A. *Adv. Mater.* **1992**, *4*, 612–649.
- (2) (a) Mezzi, G.; Zaleski, C. M.; Pecoraro, V. L. *Chem. Rev.* **2007**, *107*, 4933–5003. (b) Brechin, E. K. *Chem. Commun.* **2005**, 5141–5153. (c) Christou, G.; Gatteschi, D.; Hendrickson, D. N.; Sessoli, R. *MRS Bull.* **2000**, *25*, 66–71.
- (3) Shibusaki, M., Yamamoto, Y., Eds.; *Multimetallic Catalysts in Organic Synthesis*; Wiley-VCH: Weinheim, Germany, 2004.
- (4) (a) Ohki, Y.; Ikagawa, Y.; Tatsumi, K. *J. Am. Chem. Soc.* **2007**, *129*, 10457–10465. (b) Laplaza, C. E.; Holm, R. H. *J. Am. Chem. Soc.* **2001**, *123*, 10255–10264.

- (5) Recent examples: (a) Feltham, H. L. C.; Brooker, S. *Coord. Chem. Rev.* **2009**, *293*, 1458–1475. (b) Lan, Y.; Novitchi, G.; Clérac, R.; Tang, J.-K.; Madhu, N. T.; Hewitt, I. J.; Anson, C. E.; Brooker, S.; Powell, A. K. *Dalton Trans.* **2009**, 1721–1727. (c) Kleij, A. W. *Chem.—Eur. J.* **2008**, *14*, 10520–10529. (d) Niel, V.; Milway, V. A.; Dawe, L. N.; Grove, H.; Tandon, S. S.; Abedin, T. S. M.; Kelly, T. L.; Spencer, E. C.; Howard, J. A. K.; Collins, J. L.; Miller, D. O.; Thompson, L. K. *Inorg. Chem.* **2008**, *47*, 176–189. (e) Schemberg, J.; Schneider, K.; Demmer, U.; Warkentin, E.; Müller, Ermller, U. *Angew. Chem., Int. Ed.* **2007**, *46*, 2408–2413. (f) Nabeshima, T.; Miyazaki, H.; Iwasaki, A.; Akine, S.; Saiki, T.; Ikeda, C. *Tetrahedron* **2007**, *63*, 3328–3333. (g) Zheng, N.; Lu, H.; Bu, X.; Feng, P. *J. Am. Chem. Soc.* **2006**, *128*, 4528–4529. (h) Artuso, F.; D'Archivio, A. A.; Lora, S.; Jerabek, K.; Králik, M.; Corain, B. *Chem.—Eur. J.* **2003**, *9*, 5292–5296. (i) Aromí, G.; Gamez, P.; Roubeau, O.; Kooijman, H.; Spek, A. L.; Driessens, W. L.; Reedijs, J. *Angew. Chem., Int. Ed.* **2002**, *41*, 1168–1170. (j) Fontecha, J. B.; Goetz, S.; McKee, V. *Angew. Chem., Int. Ed.* **2002**, *41*, 4553–4556. (k) Che, C.-M.; Xia, B.-H.; Huang, J.-S.; Chan, C.-K.; Zhou, Z.-Y.; Cheung, K.-K. *Chem.—Eur. J.* **2001**, *7*, 3998–4006. (l) Laplaza, C. E.; Holm, R. H. *J. Am. Chem. Soc.* **2001**, *123*, 10255–10264. (m) Doble, D. M. J.; Benison, C. H.; Blake, A. J.; Fenske, D.; Jackson, M. S.; Kay, R. D.; Li, W.-S.; Schröder, M. *Angew. Chem., Int. Ed.* **1999**, *38*, 1915–1918.
- (6) Einsle, O.; Tezcan, F. A.; Andrade, S. L. A.; Schmid, B.; Yoshida, M.; Howard, J. B.; Rees, D. C. *Science* **2002**, *297*, 1696–1700.

Chart 1. Tris(salphen) [3 + 3] Schiff Base Macrocycles **1a–e**

variety of organic transformations.⁷ Often synergy between metal ions imparts improved regio-selectivity or rate enhancements compared to similar monometallic catalysts. To expedite the discovery of novel multimetallic catalysts and enzyme mimics, more reliable strategies for controlling geometry, composition, and nuclearity of metal clusters are needed.

Developing template-assisted routes to hetero- and homopoly-metallic clusters is of interest to us. In particular, our research efforts have focused on the coordination chemistry of tris(salphen) Schiff base macrocycle **1** shown in Chart 1.⁸ When **1** was reacted with an excess of zinc acetate, a heptazinc cluster supported by the macrocyclic scaffold was isolated.⁹ We later confirmed macrocycle **1** acts as a template for the growth of heptazinc clusters and that isolable, reactive tetrazinc intermediates are good precursors for the formation of mixed-metal Zn₄Co₃ and Zn₃Co₄ clusters.¹⁰ Nabeshima et al. demonstrated that the cluster-capping Zn₄O tetrahedron, supported by six acetate ligands, may be released from the template upon addition of La³⁺ ions, suggesting these macrocyclic templates can steer polymetallic cluster formation then deliver the cluster upon addition of an external stimulus.¹¹

Interestingly, the Zn₄O cluster templated by macrocycle **1** closely resembles a tetrametallic Zn₄(CF₃COO)₆O catalyst discovered by Ohshima et al. that promotes the acylation of hydroxyl groups over amines with selectivities up to 99% in some cases.¹² The same catalyst provides a facile route for the direct conversion of esters, lactones, and carboxylic acids to

- (7) (a) Shibusaki, M.; Matsunaga, S.; Kumagai, N. *Synlett* **2008**, 1583–1602. (b) Gianneschi, N. C.; Masar, M. S.; Mirkin, C. A. *Acc. Chem. Res.* **2005**, 38, 825–837. (c) Roundhill, D. M.; Dickson, M. K.; Dixit, N. S.; Sudha-Dixit, B. P. *J. Am. Chem. Soc.* **1980**, 102, 5538–5542.
- (8) (a) Shopowitz, K. E.; Edwards, D.; Gallant, A. J.; MacLachlan, M. J. *Tetrahedron* **2009**, 65, 8113–8119. (b) MacLachlan, M. J. *Pure Appl. Chem.* **2006**, 78, 873–888. (c) Gallant, A. J.; Hui, J.K.-H.; Zahariev, F. E.; Wang, Y. A.; MacLachlan, M. J. *J. Org. Chem.* **2005**, 70, 7936–7946. (d) Gallant, A. J.; Yun, M.; Sauer, M.; Yeung, C. S.; MacLachlan, M. J. *Org. Lett.* **2005**, 7, 4827–4830. (e) Ma, C. T. L.; MacLachlan, M. J. *Angew. Chem., Int. Ed.* **2005**, 44, 4178–4182. (f) Gallant, A. J.; MacLachlan, M. J. *Angew. Chem., Int. Ed.* **2003**, 42, 5307–5310. (g) Akine, S.; Taniguchi, T.; Nabeshima, T. *Tetrahedron Lett.* **2001**, 42, 8861–8864. (h) Huck, W. T. S.; van Veggel, F. C. J. M.; Reinhoudt, D. N. *Recl. Trav. Chim. Pays-Bas* **1995**, 114, 273–276.
- (9) Gallant, A. J.; Chong, J. H.; MacLachlan, M. J. *Inorg. Chem.* **2006**, 45, 5248–5250.
- (10) Frischmann, P. D.; Gallant, A. J.; Chong, J. H.; MacLachlan, M. J. *Inorg. Chem.* **2008**, 47, 101–112.
- (11) Nabeshima, T.; Miyazaki, H.; Iwasaki, A.; Akine, S.; Saiki, T.; Ikeda, C.; Sato, S. *Chem. Lett.* **2006**, 35, 1070–1071.

oxazolines in the presence of an amino alcohol.¹³ Inspired by the catalytic utility of Zn₄(CF₃COO)₆O clusters and their structural similarity to hepta-zinc clusters templated by macrocycle **1**, we have explored the versatility of macrocycle **1** as a template for novel molecular cadmium carboxylate clusters.

Cadmium chalcogenide materials are well-known for their semiconducting properties, and molecular cadmium sulfide or selenide clusters have frequently been isolated.¹⁴ When carboxylates are coordinated to Cd²⁺ ions, infinite mononuclear 2D and 3D metal–organic frameworks (MOFs) are obtained.¹⁵ In a few cases cadmium carboxylate MOFs are constructed of high nuclearity (>4 Cd²⁺ ions) secondary building units.¹⁶ However, to our knowledge there is only one report of a high nuclearity molecular cadmium carboxylate cluster: a decacadmium wheel-shaped cluster that was only characterized in the solid state.¹⁷ Supported by phosphonates and not carboxylates, the molecular icosacadmium cluster reported by Roesky and co-workers is the largest O-donor supported molecular cadmium cluster reported to date.¹⁸

Reacting macrocycle **1** with cadmium acetate yields a heptacadmium cluster complex that dimerizes, forming capsules both in solution and in the solid state.¹⁹ Since metal coordination

- (12) (a) Ohshima, T.; Iwasaki, T.; Maegawa, Y.; Yoshiyama, A.; Mashima, K. *J. Am. Chem. Soc.* **2008**, 130, 2944–2945. (b) Transesterification study: Iwasaki, T.; Maegawa, Y.; Hayashi, Y.; Ohshima, T.; Mashima, K. *J. Org. Chem.* **2008**, 73, 5147–5150.
- (13) Ohshima, T.; Iwasaki, T.; Mashima, K. *Chem. Commun.* **2006**, 2711–2713.
- (14) (a) Sanville, E.; Burnin, A.; BelBruno, J. *J. Phys. Chem. A* **2006**, 110, 2378–2386. (b) DeGroot, M. W.; Taylor, N. J.; Corrigan, J. F. *Inorg. Chem.* **2005**, 44, 5447–5458. (c) Behrens, S.; Bettenhausen, M.; Eichhöfer, A.; Fenske, D. *Angew. Chem., Int. Ed.* **1997**, 36, 2797–2799. (d) Behrens, S.; Bettenhausen, M.; Deveson, A. C.; Eichhöfer, A.; Fenske, D.; Lohde, A.; Woggon, U. *Angew. Chem., Int. Ed.* **1996**, 35, 2215–2218. (e) Jin, X.; Tang, K.; Jia, S.; Tang, Y. *Polyhedron* **1996**, 15, 2617–2622. (f) Dance, I. G.; Choy, A.; Scudder, M. L. *J. Am. Chem. Soc.* **1984**, 106, 6285–6295.
- (15) Recent examples: (a) Liang, X.-Q.; Zhou, X.-H.; Chen, C.; Xiao, H.-P.; Li, Y.-Z.; Zuo, J.-L.; You, X.-Z. *Cryst. Growth Des.* **2009**, 9, 1041–1053. (b) Wei, G.-H.; Yang, J.; Ma, J.-F.; Liu, Y.-Y.; Li, S.-L.; Zhang, L.-P. *Dalton Trans.* **2008**, 3080–3092. (c) Liu, G.-X.; Huang, R.-Y.; Xu, H.; Kong, X.-J.; Huang, L.-F.; Zhu, K.; Ren, X.-M. *Polyhedron* **2008**, 27, 2327–2336. (d) Yao, Y.-L.; Che, Y.-X.; Zheng, J.-M. *Inorg. Chem. Commun.* **2008**, 11, 1253–1255. (e) Shi, Q.; Sun, Y.; Sheng, L.; Ma, K.; Hu, M.; Hu, X.; Huang, S. *Cryst. Growth Des.* **2008**, 8, 3401–3407. (f) Chen, Z.-F.; Zhang, Z.-L.; Tan, Y.-H.; Tang, Y.-Z.; Fan, H.-K.; Zhou, Z.-Y.; Abrahams, B. F.; Liang, H. *CrystEngComm* **2008**, 10, 217–231. (g) Wang, L.; Yang, M.; Li, G.; Shi, Z.; Feng, S. *Inorg. Chem.* **2006**, 45, 2474–2478. (h) Wu, J.-Y.; Chang, C.-H.; Tseng, T.-W.; Lu, K.-L. *J. Mol. Struct.* **2006**, 796, 69–75. (i) Xiong, R.-G.; You, X.-Z.; Abrahams, B. F.; Xue, Z.; Che, C.-M. *Angew. Chem., Int. Ed.* **2001**, 40, 4422–4425. (j) Kim, J.; Chen, B.; Reineke, T. M.; Li, H.; Eddaoudi, M.; Moler, D. B.; O’Keeffe, M.; Yaghi, O. M. *J. Am. Chem. Soc.* **2001**, 123, 8239–8247.
- (16) (a) Wang, X.-L.; Qin, C.; Lan, Y.-Q.; Shao, K.-Z.; Su, Z.-M.; Wang, E.-B. *Chem. Commun.* **2009**, 410–412. (b) Xiao, D.; Yuan, R.; Chai, Y.; Wang, E. *Eur. J. Inorg. Chem.* **2008**, 2610–2615. (c) Fang, Q.-R.; Zhu, G.-S.; Jin, Z.; Xue, M.; Wei, X.; Wang, D.-J.; Qiu, S.-L. *Angew. Chem., Int. Ed.* **2006**, 45, 6126–6130. (d) Chun, H.; Kim, D.; Dybtsev, D. N.; Kim, K. *Angew. Chem., Int. Ed.* **2004**, 43, 971–974. (e) Tao, J.; Yin, X.; Wei, Z.-B.; Huang, R.-B.; Zheng, L.-S. *Eur. J. Inorg. Chem.* **2004**, 125–133. (f) Zheng, S.-L.; Yang, J.-H.; Yu, X.-L.; Chen, X.-M.; Wong, W.-T. *Inorg. Chem.* **2004**, 43, 830–838. (g) Wang, X.-L.; Qin, C.; Wang, E.-B.; Xu, L.; Su, Z.-M.; Hu, C.-W. *Angew. Chem., Int. Ed.* **2004**, 43, 5036–5040. (h) Wang, R.; Hong, M.; Luo, J.; Cao, R.; Weng, J. *Chem. Commun.* **2003**, 1018–1019.
- (17) Liu, Y.; Hou, H.; Chen, Q.; Fan, Y. *Cryst. Growth Des.* **2008**, 8, 1435–1442.
- (18) Anantharaman, G.; Walawalkar, M. G.; Murugavel, R.; Gábor, B.; Herbst-Irmer, R.; Baldus, M.; Angerstein, B.; Roesky, H. W. *Angew. Chem., Int. Ed.* **2003**, 42, 4482–4485.
- (19) Frischmann, P. D.; MacLachlan, M. J. *Chem. Commun.* **2007**, 4480–4482.

induces the otherwise planar macrocycle to adopt a bowl-like conformation, we have dubbed it a *metallocavatand*.²⁰ From crystallography, ¹H NMR spectroscopy, and DFT calculations we have discovered an unusual μ_3 -hydroxo ligand that is located deep inside each cavity and able to form hydrogen bonds with encapsulated guests. This article describes our recent investigations of supramolecular self-assembly, cadmium carboxylate metal cluster dynamics, and solid-state guest dynamics of heptacadmium metallocavatands using DFT, X-ray crystallography, and variable temperature solution and solid-state NMR spectroscopy.

Methods

Chemicals. Macrocycles **1a–d**,^{8c,10} and metallocavatands **2a** and **2d**¹⁹ were prepared by previously reported methods. Full details of the synthesis and characterization of **2b** and **2c** are provided in the Supporting Information.

Instrumentation. X-ray crystallography, NMR spectroscopy, mass spectrometry, UV-vis spectroscopy, and IR spectroscopy were carried out on commercially available instruments using standard procedures as described in the Supporting Information.

Solid-State ²H NMR Spectroscopy. The ²H NMR spectra were measured on a Bruker ASX 200 NMR spectrometer equipped with a 5 mm wide-line solenoid probe operating at 30.7 MHz for ²H. The quadrupolar echo sequence²¹ was used to collect the data with 2k complex points in the FID using a spectral width of 1 MHz. Each spectrum was the signal average of 600–800 transients. The 90° pulses were 3.5 μ s and the recycle delay was 5 s. The first and second echo delays were set to 35 and 33 μ s, respectively. The time domain data were left-shifted to locate the top of the echo and an exponential line broadening of 200 Hz was applied prior to Fourier transformation. The temperature was lowered by passing dry nitrogen gas through a heat exchanger coil immersed in liquid nitrogen. The cold gas was heated to the desired temperature with the heater in the NMR probe and controlled by the variable temperature control unit of the spectrometer which uses a thermocouple in the vicinity of the coil to regulate the temperature. The precise temperature of the sample was measured after the NMR measurement by placing a thermocouple directly on the coil of the NMR probe. Reported temperatures are thought to be accurate and precise to within 1 K. The simulations were conducted using NMR-WEBLAB V4.1.2.²²

Computational Details. To support the experimental results, density functional theory (DFT) calculations were performed using the ADF2007²³ and Gaussian03 (revision D.02)²⁴ packages. The ADF2007 program allowed explicit consideration of relativistic effects using the zero order regular approximation (ZORA) approach.²⁵ This variationally stable scheme is based on a regular-potential expansion and produces a Hamiltonian that in zeroth order reproduces all important relativistic effects including the spin-orbit interaction.

A valence triple- ζ STO basis set with one polarization function (ZORA/TZP without frozen cores) was used for the relativistic

calculations. Gradient corrected exchange-correlation (xc) functionals of Perdew, Burke, and Ernzerhof (PBE)²⁶ have been used. The local part of the xc functionals was the default Vosko, Wilk and Nusair (VWN)²⁷ one. Integration accuracy has been increased to 10⁻⁸ (using keyword “INTEGRATION 8.0”) and Self Consistent Field convergence criterion has been chosen equal to 10⁻⁹ (keyword “SCF”, subkey “converge 1e-9”). Structures have been fully optimized^{28,29} without using symmetry constraints and applying default convergence criteria apart from the maximum gradient which has been set to 10⁻⁴ hartree/bohr. Delocalized coordinates have been used (“delocal” option).

In the case of Gaussian 03 computations the DFT has been applied using both pure PBE²⁶ and the hybrid B98³⁰ or PBE1PBE³¹ xc functionals. Geometry optimizations have been performed by using both the 3-21g³² and Dunning/Huzinaga valence double- ζ (D95V(d,p)) basis sets,³³ adding a set of polarization functions to the same basis set in case of H, C, N, and O. The Stuttgart/Dresden ECP basis set³⁴ and pseudopotential (SDD) including relativistic effects have been used for Cd atoms.

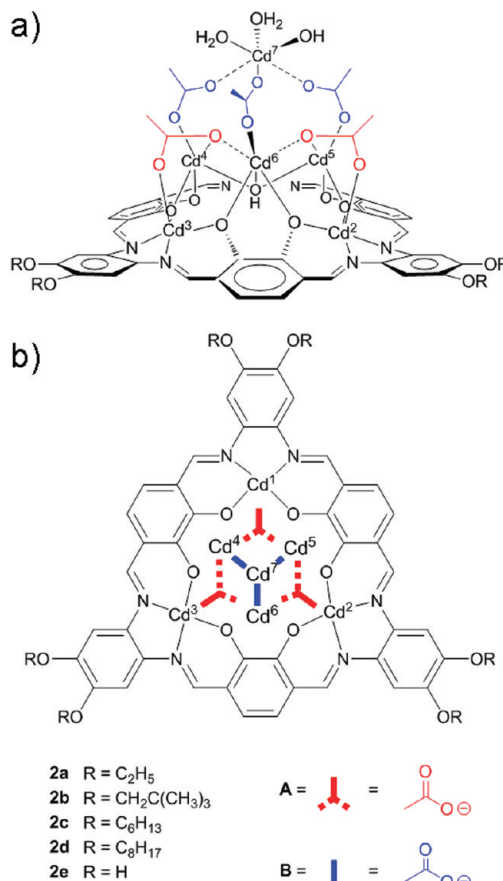
In the study of the rotation of the DMF molecule when H-bonded to the μ_3 -OH ligand of **2e**, the 6-31g(d,p)³⁵ basis set was used for the H, C, N, and O atoms of DMF and μ_3 -OH in order to better describe the H-bonding interaction. The 3-21g basis set was used for all remaining H, C, N, and O atoms. Basis set superposition error (BSSE)^{36,37} contributions to the interaction energies have been corrected by means of the Boys and Bernardi counterpoise³⁶ (CP) approach. These corrections ranged from 28% to 39% of the value of the interaction energy.

Default gradient and displacement thresholds have been used for the geometry optimization convergence criteria.

To confirm that the obtained geometries are relative minima of the potential energy surface (electronic energy in the Born–Oppenheimer approximation + internuclear repulsion energy), analytical computation of the Hessian matrix with respect to the nuclear coordinates at the same level of theory was performed.

- (25) (a) van Lenthe, E.; Ehlers, A.; Baerends, E. J. *J. Chem. Phys.* **1999**, *110*, 8943–8953. (b) van Lenthe, E.; Baerends, E. J.; Snijders, J. G. *J. Chem. Phys.* **1993**, *99*, 4597–4610. (c) van Lenthe, E.; Baerends, E. J.; Snijders, J. G. *J. Chem. Phys.* **1994**, *101*, 9783–9792. (d) van Lenthe, E.; van Leeuwen, R.; Baerends, E. J.; Snijders, J. G. *Int. J. Quantum Chem.* **1996**, *57*, 281–293.
- (26) Perdew, J. P.; Burke, K.; Ernzerhof, M. *Phys. Rev. Lett.* **1996**, *77*, 3865–3868.
- (27) Vosko, S. H.; Wilk, L.; Nusair, M. *Can. J. Phys.* **1980**, *58*, 1200–1211.
- (28) Schlegel, H. B. *J. Comput. Chem.* **1982**, *3*, 214–218.
- (29) Schlegel, H. B. Geometry Optimization on Potential Energy Surfaces. In *Modern Electronic Structure Theory*; Yarkony, D. R., Ed.; World Scientific Publishing: Singapore, 1995; Vol. 2, pp 459–500.
- (30) Schmid, H. L.; Becke, A. D. *J. Chem. Phys.* **1998**, *108*, 9624–9631.
- (31) Adamo, C.; Barone, V. *J. Chem. Phys.* **1999**, *110*, 6158–6170.
- (32) (a) Binkley, J. S.; Pople, J. A.; Hehre, W. J. *J. Am. Chem. Soc.* **1980**, *102*, 939–947. (b) Gordon, M. S.; Binkley, J. S.; Pople, J. A.; Pietro, W. J.; Hehre, W. J. *J. Am. Chem. Soc.* **1982**, *104*, 2797–2803. (c) Pietro, W. J.; Franci, M. M.; Hehre, W. J.; Defrees, D. J.; Pople, J. A.; Binkley, J. S. *J. Am. Chem. Soc.* **1982**, *104*, 5039–5048. (d) Dobbs, K. D.; Hehre, W. J. *J. Comput. Chem.* **1986**, *7*, 359–378. (e) Dobbs, K. D.; Hehre, W. J. *J. Comput. Chem.* **1987**, *8*, 861–879. (f) Dobbs, K. D.; Hehre, W. J. *J. Comput. Chem.* **1987**, *8*, 880–893.
- (33) Dunning Jr., T. H.; Hay, P. J. in *Modern Theoretical Chemistry*; Schaefer, H. F., III, Ed.; Plenum: New York, 1976; Vol. 3, pp 1–28.
- (34) Nicklass, A.; Dolg, M.; Stoll, H.; Preuss, H. *J. Chem. Phys.* **1995**, *102*, 8942–8952, and references therein.
- (35) (a) Ditchfield, R.; Hehre, W. J.; Pople, J. A. *J. Chem. Phys.* **1971**, *54*, 724–728. (b) Hehre, W. J.; Ditchfield, R.; Pople, J. A. *J. Chem. Phys.* **1972**, *56*, 2257–2261. (c) Hariharan, P. C.; Pople, J. A. *Mol. Phys.* **1974**, *27*, 209–214. (d) Gordon, M. S. *Chem. Phys. Lett.* **1980**, *76*, 163–168. (e) Hariharan, P. C.; Pople, J. A. *Theor. Chim. Acta* **1973**, *28*, 213–222.
- (36) Boys, S. F.; Bernardi, F. *Mol. Phys.* **1970**, *19*, 553–566.
- (37) Simon, S.; Duran, M.; Dannenberg, J. J. *J. Chem. Phys.* **1996**, *105*, 11024–11031.

Chart 2. Depiction of Heptacadmium Complexes **2a–e** with the Two Distinct Acetate Environments Labeled A (Red) or B (Blue)^a



^a (a) Side-on representation. Cd¹, the third dialkoxyphenylenediamine unit, and one type-A acetate are obscured by the cluster. (b) Top-down representation of **2a–e** highlighting the acetate-Cd connectivity.

In the case of the macrocyclic ligand **1e**, time dependent DFT (TD-DFT)³⁸ calculations of the UV spectrum were performed at the D95V(d,p)/PBE1PBE1 level of theory.

Structures and the Kohn–Sham orbitals have been drawn with the program GaussView3.0 and MOLEKEL4.3.³⁹

Results and Discussion

Synthesis and Characterization. Stirring seven equivalents of Cd(OAc)₂•2H₂O in a suspension of macrocycle **1a–d** in MeOH or EtOH followed by filtration yields metallocavitands **2a–d** in 57–75% yield with no further purification necessary.⁴⁰ Metallocavitands **2a** and **2b** have been studied in the solid state by single-crystal X-ray diffraction (SCXRD) and experimental evidence strongly indicates that metallocavitands **2a–d** share the core structure depicted in Chart 2.

NMR spectra of metallocavitands **2a–b** were recorded in DMF-*d*₇ whereas for the more soluble **2c–d**, spectra were recorded in CDCl₃. Like their parent macrocycles, **2a–d** have

(38) (a) Casida, M. E. Time dependent density functional response theory for molecules, In *Recent Advances in Density Functional Methods, Pt. I*; Chong, D. P., Ed.; World Scientific: Singapore, 1995; Vol. 1, p 155. (b) Casida, M. E.; Jamorski, C.; Casida, K. C.; Salahub, D. R. *J. Chem. Phys.* **1998**, *108*, 4439–4449.

(39) Flügge, P.; Lüthi, H. P.; Portmann, S.; Weber, J. MOLEKEL 4.3; Swiss Center for Scientific Computing, Manno, Switzerland, 2000.

(40) The synthesis of metallocavitands **2a** and **2d** was previously communicated in reference 19.

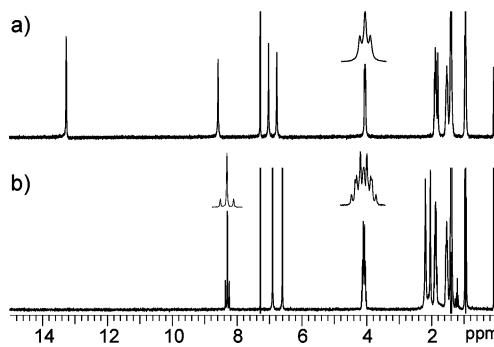


Figure 1. ¹H NMR spectra before and after heptacadmium metallocavitand formation: (a) macrocycle **1c** with the triplet OCH₂ resonance inset and (b) metallocavitand **2c** showing the imine resonance with 34.1 Hz ³J_{Cd–H} satellites and the ABX₂ coupling observed for the OCH₂ resonance inset. (400 MHz, CDCl₃; residual CHCl₃ is at 7.27 ppm.)

*C*₃ rotational symmetry in solution resulting in greatly simplified NMR spectra. The most diagnostic resonances in the ¹H NMR spectrum of **2c** (Figure 1) are the imine and OCH₂ methylene resonances found around 8.26 and 4.05 ppm, respectively. Upon metalation, three prominent changes from macrocycle **1c** are noteworthy in the proton NMR spectrum: (1) downfield OH resonances are absent, (2) three bond ¹¹¹/¹¹³Cd–H *J*-coupling is observed for the imine resonance, and (3) OCH₂ methylene resonances show a complex ABX₂ coupling pattern. The first two changes confirm metalation of the N₂O₂ salphen pockets while the diastereotopic nature of the OCH₂ methylene resonances indicates the horizontal mirror plane present in the parent macrocycle has been lost, effectively switching the symmetry from *D*_{3h} in the macrocycle to *C*_{3v} in the cadmium product. Identical spectral changes are observed for metallocavitands **2a–d** with one exception: the OCH₂ methylene resonance of **2b** is a broad singlet rather than two doublets due to a dynamic process discussed later in the text.

Both ¹¹¹Cd and ¹¹³Cd isotopes have nearly identical NMR spectroscopic characteristics, so we arbitrarily chose ¹¹³Cd for this study. Three separate ¹¹³Cd resonances were located at 139.5, 10.1, and 1.1 ppm in the ¹H-coupled ¹¹³Cd NMR spectrum of **2c** and integration gave a 3:1:3 ratio, respectively. We assigned the resonance at 139.5 ppm to cadmium ions 1–3 because of the 34.1 Hz ³J_{Cd–H} coupling constant, in agreement with the coupling observed for the imine resonance in the ¹H NMR spectrum. Since the spectrum was collected with a reasonably long delay between pulses (30 s) we trusted the integration and assigned the resonances at 10.1 and 1.1 ppm to Cd⁷ and Cd^{4–6}, respectively.

Mass spectrometry of metallocavitands **2a–d** was problematic with the best results being obtained by matrix assisted laser desorption ionization time-of-flight mass spectrometry (MALDI-TOF MS). From separate experiments, diagnostic peaks were found at *m/z* = 2383.5, 2130.9, and 2465.7 corresponding to [2b-(H₂O)₂OH]⁺, [2c-(H₂O)₂(OH)₂Cd₂(OAc)₂+Na]⁺, and [2c-(H₂O)₂OH]⁺, respectively. Peaks were found near the expected position for the molecular ion in the spectra of **2a** and **2d**; however, none could be assigned.

Both parent macrocycles **1a–d** and metallocavitands **2a–d** are isolated as orange to deep red powders that yield deep red solutions when dissolved in a variety of solvents. The electronic absorption spectra of **2a–d** are very similar with two absorption maxima found around 350 and 412 nm in CH₂Cl₂. We hypothesize that these absorptions are due to π–π* transitions

since they are shared with their parent macrocycles and have extinction coefficients with magnitudes around 10^4 to 10^5 L mol $^{-1}$ cm $^{-1}$. In agreement with our hypothesis, the difference among the D95V(d,p)/SDD/PBE1PBE DFT computed energies of the three π highest occupied orbitals and the two lowest π^* unoccupied orbitals, LUMO and LUMO+1, of **2e** give a group of wavelengths in the range 403–407 nm. Furthermore, the difference between the energy of the same three highest occupied orbitals and that of the π^* LUMO+2 gives values of wavelength in the range 279–281 nm. Differences among energies of orbitals below HOMO-3 and LUMO and LUMO+1 or between orbitals HOMO-2, HOMO-1, HOMO, and orbitals higher in energy than LUMO+2 correspond to even shorter wavelengths. This indication is further supported by a study^{8c} performed at semiempirical level and by the present TD-DFT computed UV spectrum of **1e** in the minimum energy C_{3v} structure that is the most similar to the macrocycle ligand conformation in the complex **2e**. The calculated transitions⁴¹ are in the ranges 377–447 nm and 327–358 nm and show multideterminantal contributions that involve a combination of excitations only among the previous set of π and π^* orbitals. These findings suggest that also in case of **2e** the two observed bands arise from $\pi-\pi^*$ transitions⁴² and that the disagreement between the computed and the experimental wavelength of the 350 nm band might be related to the fact that we simply used differences between monoelectronic energies.

The most notable resonance in the IR spectra of **2a–d** is the imine stretching mode found between 1606 and 1617 cm $^{-1}$. Values within this range are common for metalated salphen.

SCXRD Analysis. Solid-state structures of metallocavatands **2a** and **2b** are very similar with a few striking differences. Two separate crystals of **2a** have been studied by SCXRD: the first was grown from hot DMF⁴³ and the second from a mixture of DMF, CH₂Cl₂, CHCl₃, and MeOH.⁴⁴ Nearly identical results were obtained for the two SCXRD experiments. The structure of **2a**, shown in Figure 2, has a high degree of symmetry, belonging to the rhombohedral space group $R\bar{3}m$. Each unit cell contains six metallocavatands organized into interlocking dimers with electron density corresponding to two DMF molecules located inside each capsule.⁴⁵ Disorder prevented the orientation of encapsulated DMF molecules from being determined by crystallography. We initially believed only one DMF could fit inside each capsule based on packing coefficients (0.40 for one

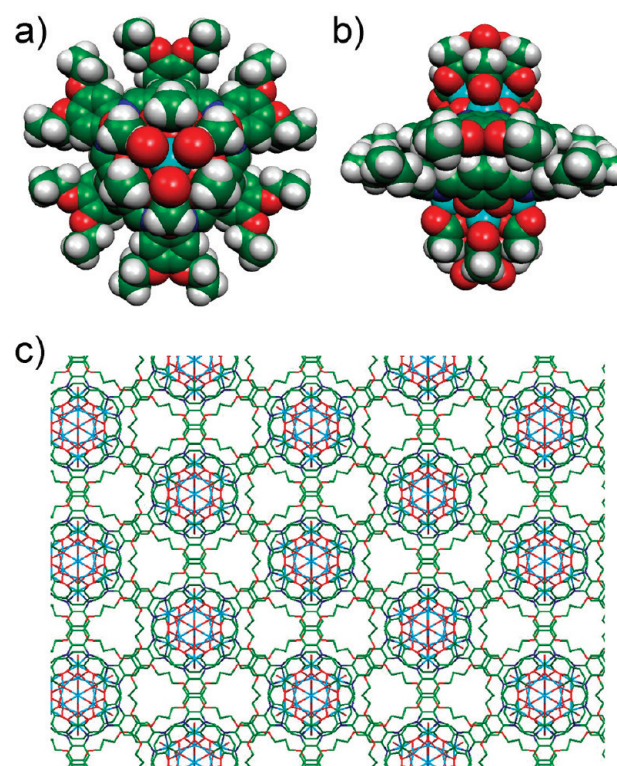


Figure 2. Capsular assembly adopted by metallocavatand **2a** ($R = \text{CH}_2\text{CH}_3$) in the solid state. (a) Top-down view of the dimer. (b) Side-on view of the dimer. (c) Hexagonal long-range packing (view down the c axis of the unit cell). (green = C, white = H, blue = N, red = O, cyan = Cd.)

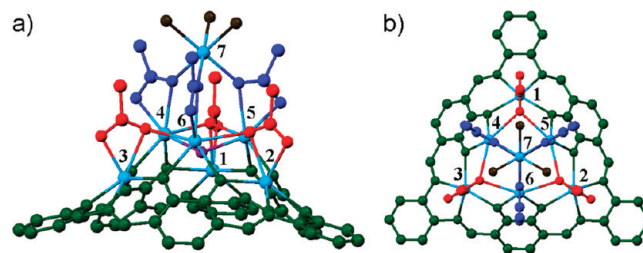


Figure 3. Solid-state structure of **2a** focusing on the $[\text{Cd}_7(\mu_3-\text{OH})(\text{OAc})_6(\text{H}_2\text{O})_2\text{OH}]$ cluster with the peripheral OEt substituents omitted. The acetate colors and cadmium labels are from Chart 2. (a) Side-on view. (b) Top-down view. (green = C, O, and N in the macrocyclic scaffold, cyan = Cd, brown = O aqua/hydroxo ligands, purple = central μ_3 -OH ligand, red = type-A acetate, blue = type-B acetate.)

(41) See SI for a comparison between the experimental and computed spectrum and tabulated computed electronic transitions.

(42) See SI for plot of the orbitals.

(43) X-ray crystal data for **2a**, 1st crystal: ($R = \text{CH}_2\text{CH}_3$): $C_{87}\text{H}_{121}\text{Cd}_{13}\text{N}_{13}\text{O}_{35}$, $M_r = 2695.77$ g mol $^{-1}$, red plate ($0.25 \times 0.25 \times 0.10$ mm 3), rhombohedral, space group $R\bar{3}m$, $a = b = 28.712(3)$, $c = 26.128(3)$ Å, $V = 18654(4)$ Å 3 , $Z = 6$, $\rho_{\text{calcd}} = 1.440$ g cm $^{-3}$, $F_{000} = 8100$, Mo K α radiation, $\lambda = 0.71069$ Å, $T = 173(2)$ K, $2\theta_{\text{max}} = 45.0^\circ$, 46300 reflections collected, 2884 unique ($R_{\text{int}} = 0.1841$). Final GoF = 1.005, $R_1 = 0.0665$, $wR_2 = 0.1847$, R indices based on 1816 reflections with $I > 2\sigma(I)$. This structure has 7 DMF molecules added into the formula.

(44) X-ray crystal data for **2a**, 2nd crystal: ($R = \text{CH}_2\text{CH}_3$): $C_{33}\text{H}_{33}\text{Cd}_{3.5}\text{N}_{3}\text{O}_{14}$, $M_r = 1089.2$ g mol $^{-1}$, red plate ($0.35 \times 0.30 \times 0.20$ mm 3), rhombohedral, space group $R\bar{3}m$, $a = b = 28.712(5)$, $c = 26.128(5)$ Å, $V = 18654(6)$ Å 3 , $Z = 12$, $\rho_{\text{calcd}} = 1.163$ g cm $^{-3}$, $F_{000} = 6384$, Mo K α radiation, $\lambda = 0.71069$ Å, $T = 173(2)$ K, $2\theta_{\text{max}} = 53.70^\circ$, 78323 reflections collected, 9612 unique ($R_{\text{int}} = 0.0618$). Final GoF = 1.011, $R_1 = 0.0911$, $wR_2 = 0.2992$, R indices based on 2850 reflections with $I > 2\sigma(I)$.

(45) PLATON/SQUEEZE results show ~80 electrons located inside the capsules of **2a**: Spek, A. L. *J. Appl. Crystallogr.* **2003**, *36*, 7–13.

vs 0.80 for two);⁴⁶ however, our results reported here strongly support the presence of two DMF molecules per capsule in the solid state. Each face-to-face capsule is formed by rotating one 3-fold symmetric metallocavatand by 60° resulting in interdigititation of the peripheral phenylenediimine units. To better describe an individual metallocavatand, the label scheme from Chart 2 will be used in the following discussion.

Figure 3 shows the connectivity of the neutral, acetate-supported, heptacadmium cluster in **2a**. Cadmium ions 1–3 occupy the salphen-like N_2O_2 pockets and their geometry may be described as distorted trigonal prismatic or distorted pentagonal pyramidal. The fifth and sixth coordination sites of cadmium ions 1–3 are occupied by one type-A acetate in a

(46) The packing coefficient is the volume ratio of guest compound to host cavity. See Mecozzi, S.; Rebek, J., Jr. *Chem.—Eur. J.* **1998**, *4*, 1016–1022.

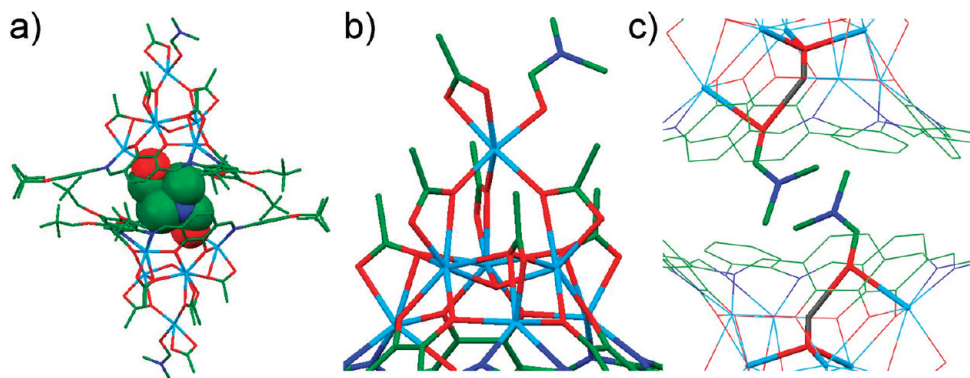


Figure 4. Crystal structure of metallocavatand **2b** ($R = \text{CH}_2\text{C}(\text{CH}_3)_3$) with the cluster-capping aqua and hydroxo ligands replaced by an acetate ligand and DMF. The homodimer that is isostructural to **2a** is also present in the unit cell but is omitted from this figure. (a) Capsule with two guest DMF molecules space filling. (b) Close up view of the cluster with the capping hydroxo and two aqua ligands replaced by a DMF (O-bound) and a bidentate acetate ligand. (c) Close-up view of the encapsulated DMF molecules with the carbonyl O–Cd bond and a potential H-bond to the μ_3 -OH ligand highlighted. The neopentyloxy chains have been omitted for clarity (green = C, blue = N, red = O, cyan = Cd, gray = H).

bidentate fashion where the meridional and axial Cd–OAc bonds are 2.43 and 2.28 Å, respectively. Above the macrocycle rest cadmium ions 4–6, each supported by a catechol unit, two type-A acetates, one type-B acetate, and bridged by a central μ_3 -hydroxo ligand to give a distorted pentagonal bipyramidal coordination environment. The Cd–O bond lengths for catechol Cd–O, axial Cd–O type-B acetate, and Cd–O (μ_3 -OH) range from 2.22 to 2.28 Å whereas the meridional Cd–O type-B acetate and both Cd–O type-A acetate bonds are longer at 2.47 and 2.53 Å, respectively. Cluster-capping cadmium ion 7 has octahedral geometry imparted by one hydroxo and two aqua ligands facially coordinated and three Cd–O type-B acetate bonds.⁴⁷ The +14 charge of seven Cd²⁺ ions is balanced by the macrocyclic phenoxides (−6), six acetates (−6), one central μ_3 -hydroxo ligand (−1), and one capping hydroxo ligand (−1).

Unable to locate most of the hydrogen atoms in the SCXRD structure of **2a**, we originally reported the μ_3 -hydroxo ligand to be an oxo ligand and the three ligands capping Cd⁷ as aqua ligands.¹⁹ We were forced to reconsider the μ_3 -oxo assignment after crystals of a crude sample of neopentyloxy substituted **2b** were subjected to a SCXRD experiment. Grown in a mixture of DMF, CH₂Cl₂, CHCl₃, and byproduct AcOH,⁴⁸ the crystal of **2b** is triclinic with each unit cell consisting of four metallocavatands.⁴⁹ Surprisingly, two different metallocavatand species are cocrystallized, each in duplicate, within the unit cell. One species is analogous to the structure of **2a**; however, in the second species the capping hydroxo and two aqua ligands have been replaced by a DMF (O-bound) and a bidentate acetate ligand as shown in Figure 4. Although the solid-state structure of **2b** is relatively low resolution, the connectivity is certain. No cations were located within the unit cell to account for the negative charge of the capping acetate. A neutral complex is

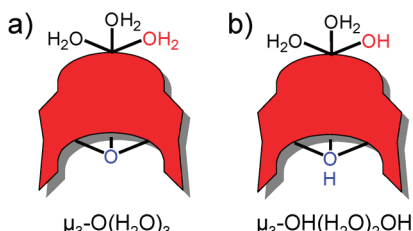
obtained only if the previously assigned, central μ_3 -oxo ligand is in fact a μ_3 -hydroxo ligand.

The two cocrystallized species of metallocavatand **2b** exist as homodimers and each dimer encapsulates two DMF molecules related by an inversion center.⁵⁰ Inside each capsule the carbonyl oxygen of DMF is weakly coordinating to cadmium (2.5–2.7 Å Cd–O) and potentially hydrogen-bonding with the μ_3 -OH ligand (3.1–3.2 Å O–O). Eight Lewis acid sites, including six unsaturated cadmium ions and two μ_3 -OH ligands, are accessible to encapsulated guests. A 3.1–3.3 Å distance separates the two DMF molecules, bringing them into van der Waals contact. In this Lewis acidic and sterically demanding environment these metallocavatands may act as nanosized reaction vessels if proper guests are encapsulated.⁵¹

While μ_3 -OH ligands are common in cubane clusters of the type M₄(OH)₄ where vertices of the cube alternate between metal and μ_3 -OH ligands,⁵² this coordination mode is rare for Cd²⁺ ions. From a search of the Cambridge Structural Database (CSD), 34 structures have been reported that possess a tetrahedral μ_3 -oxygen ligand bridging three cadmium ions,⁵³ 18 of those are μ_3 -OR,⁵⁴ 13 are μ_3 -OH,^{16b,d–f,17,55} and 3 are μ_3 -oxo.^{19,56} The μ_3 -O–Cd bond lengths in **2a** and **2b**, 2.22 and 2.19–2.27 Å, respectively, are essentially in the 2.20–2.41 Å range of both the hydroxo and oxo bridged structures reported in the literature. As the disorder in the crystal structures of **2a** and **2b** prevented us from accurately locating the positions of protons in the electron density maps, we turned to DFT

- (47) Aqua and hydroxo protons were not located on the difference map and the R_{3m} space group averages out the Cd–O bond lengths preventing an exact assignment.
 (48) Formation of metallocavatand **2** generates 8 equivalents of acetic acid.
 (49) X-ray crystal data for **2b** ($R = \text{CH}_2\text{C}(\text{CH}_3)_3$): C₃₉₀H₅₁₅Cd₂₈N₄₂O₁₂₈, $M_r = 10986.97$, red block ($0.70 \times 0.45 \times 0.20 \text{ mm}^3$), triclinic, space group P-1, $a = 20.083(3)$, $b = 22.576(4)$, $c = 34.101(6)$ Å, $\alpha = 81.279(9)$, $\beta = 88.262(9)$, $\delta = 82.512(9)$ °, $V = 15152(4)$ Å³, $Z = 1$, $\rho_{\text{calcd}} = 1.206 \text{ g cm}^{-3}$, $F_{000} = 5533$, Mo K α radiation, $\lambda = 0.71073$ Å, $T = 173(2)$ K, $2\theta_{\text{max}} = 44.4^\circ$, 31117 reflections collected, 31117 unique ($R_{\text{int}} = 0.000$). Final GoF = 1.113, $R_1 = 0.1158$, $wR_2 = 0.3266$, R indices based on 19376 reflections with $I > 2\sigma(I)$.

- (50) One encapsulated DMF molecule is removed after heating under vacuum for 48 h as confirmed by ¹H NMR spectroscopy in DMSO-*d*₆.
 (51) For a review: (a) Yoshizawa, M.; Klosterman, J. K.; Fujita, M. *Angew. Chem., Int. Ed.* **2009**, *48*, 3418–3438. Recent examples: (b) Crisóstomo, F. R. P.; Lledó, A.; Shenoy, S. R.; Iwasawa, T.; Rebek, J., Jr. *J. Am. Chem. Soc.* **2009**, *131*, 7402–7410. (c) Gibb, C. L. D.; Sundaresan, A. K.; Ramamurthy, V.; Gibb, B. C. *J. Am. Chem. Soc.* **2008**, *130*, 4069–4080. (d) Pluth, M. D.; Bergman, R. G.; Raymond, K. N. *Science* **2007**, *316*, 85–88.
 (52) (a) Kong, X.-J.; Wu, Y.; Long, L.-S.; Zheng, L.-S.; Zheng, Z. *J. Am. Chem. Soc.* **2009**, *131*, 6918–6919. (b) Zhao, J.-W.; Jia, H.-P.; Zhang, J.; Zheng, S.-T.; Yang, G.-Y. *Chem.–Eur. J.* **2007**, *13*, 10030–10045. (c) Zuhayra, M.; Kampen, W. U.; Henze, E.; Soti, Z.; Zsolnai, L.; Huttner, G.; Oberdorfer, F. *J. Am. Chem. Soc.* **2006**, *128*, 424–425. (d) Lee, D.; Sorace, L.; Caneschi, A.; Lippard, S. J. *Inorg. Chem.* **2001**, *40*, 6774–6781. (e) Ama, T.; Rashid, M. M.; Yonemura, T.; Kawaguchi, H.; Yasui, T. *Coord. Chem. Rev.* **2000**, *198*, 101–116.
 (53) Cambridge Structural Database (CSD) search was conducted on May 7, 2009 with ConQuest Version 1.11.

Chart 3. Prototropic Tautomers of Metallocavitand **2^a**

^a (a) The μ_3 -oxo complex with three capping aqua ligands is unstable.
 (b) The μ_3 -hydroxo species with two capping aqua ligands and a capping hydroxo ligand is the species observed.

calculations to confirm the location of any oxo, hydroxo, and/or aqua ligands in metallocavitands **2a–d**.

Computational Evidence for a μ_3 -OH Ligand and Optimized DMF-Cavity Interactions. Two possible cluster configurations were explored computationally, one with a μ_3 -oxo and the other with a μ_3 -hydroxo ligand; these prototropic tautomers are illustrated in Chart 3. DFT energy minimization at the 3-21g/SDD/PBE level of theory, without any constraints and assuming a C₁ point group symmetry, of complex **2e** (R = H) as depicted in Chart 3a (i.e., characterized by the central μ_3 -oxo ligand bonded to Cd^{1–3} atoms and three capping aqua ligands) resulted in dramatic geometrical reorganization of the cluster. In particular, two of the three water molecules dissociate and the μ_3 -oxo ligand moves toward Cd⁷ while at the same time bridging the Cd^{4–6} atoms. This rearrangement leads to a tetrahedral μ_4 -oxo coordinated to the Cd^{4–7} atoms akin to Zn clusters,^{9–11} indicating the starting μ_3 -oxo configuration is unstable. This behavior is independent of the basis set and xc functional used. Calculations verified that the central μ_3 -oxo ligand must be a μ_3 -hydroxo ligand and that the capping ligands are two aqua and one hydroxo ligand, suggesting that the structure should be that reported in Chart 3b. Computations were further

- (54) R is C in most cases but may be B, N, or P. (a) Zhu, A.-X.; Zhang, J.-P.; Lin, Y.-Y.; Chen, X.-M. *Inorg. Chem.* **2008**, *47*, 7389–7395. (b) Chakraborty, J.; Thakurta, S.; Samanta, B.; Ray, A.; Pilet, G.; Batten, S. R.; Jensen, P.; Mitra, S. *Polyhedron* **2007**, *26*, 5139–5149. (c) Chen, Z.; Liang, F.; Zhou, S.; Xia, C.; Hu, R. *J. Mol. Struct.* **2007**, *827*, 20–24. (d) Suen, M.-C.; Wang, J.-C. *Inorg. Chem. Commun.* **2006**, *9*, 478–481. (e) Lo, W.-K.; Wong, W.-K.; Wong, W.-Y.; Guo, J. *Eur. J. Inorg. Chem.* **2005**, 3950–3954. (f) Tong, M.-L.; Zheng, S.-L.; Shi, J.-X.; Tong, Y.-X.; Lee, H. K.; Chen, X.-M. *J. Chem. Soc., Dalton Trans.* **2002**, 1727–1734. (g) Vinogradova, E. A.; Vassilyeva, O. Y.; Kokozay, V. N.; Skelton, B. W.; Bjernemose, J. K.; Raithby, P. R. *J. Chem. Soc., Dalton Trans.* **2002**, 4248–4252. (h) Tong, M.-L.; Lee, H. K.; Zheng, S.-L.; Chen, X.-M. *Chem. Lett.* **1999**, *28*, 1087–1091. (i) Luliński, S.; Madura, I.; Serwatowski, J.; Zachara, J. *Inorg. Chem.* **1999**, *38*, 4937–4941. (j) Harms, K.; Merle, J.; Maichle-Mössmer, C.; Massa, W.; Krieger, M. *Inorg. Chem.* **1998**, *37*, 1099–1104. (k) Büsching, I.; Strasdeit, H. *J. Chem. Soc., Chem. Commun.* **1994**, 2789–2790. (l) Boulmaaz, S.; Papiernik, R.; Hubert-Pfalzgraf, L. G.; Vaissermann, J.; Daran, J.-C. *Polyhedron* **1992**, *11*, 1331–1336. (m) Liles, D. C.; McPartlin, M.; Tasker, P. A.; Lip, H. C.; Lindoy, L. F. *J. Chem. Soc., Chem. Commun.* **1976**, 549–551.
- (55) (a) Ouellette, W.; Hudson, B. S.; Zubietia, J. *Inorg. Chem.* **2007**, *46*, 4887–4904. (b) Poul, L.; Fakhfakh, M.; Taibi, M.; Jouini, N.; Herson, P.; Fiévet, F. *J. Chem. Crystallogr.* **2005**, *35*, 285–291. (c) Forniés, J.; Gómez, J.; Lalinde, E.; Moreno, M. T. *Inorg. Chem.* **2001**, *40*, 5415–5419. (d) Lin, W.; Wang, Z.; Ma, L. *J. Am. Chem. Soc.* **1999**, *121*, 11249–11250. (e) Duhme, A.-K.; Strasdeit, H. *Eur. J. Inorg. Chem.* **1998**, 657–662. (f) Weidenbruch, M.; Herrndorf, M.; Schäfer, A.; Pohl, S.; Saak, W. *J. Organomet. Chem.* **1989**, *361*, 139–145.
- (56) (a) Shen, X.-Q.; Yao, H.-C.; Yang, R.; Li, Z.-J.; Zhang, H.-Y.; Wu, B.-L.; Hou, H.-W. *Polyhedron* **2008**, *27*, 203–209. (b) Dai, J.-C.; Wu, X.-T.; Fu, Z.-Y.; Cui, C.-P.; Hu, S.-M.; Du, W.-X.; Wu, L.-M.; Zhang, H.-H.; Sun, R.-Q. *Inorg. Chem.* **2002**, *41*, 1391–1396.

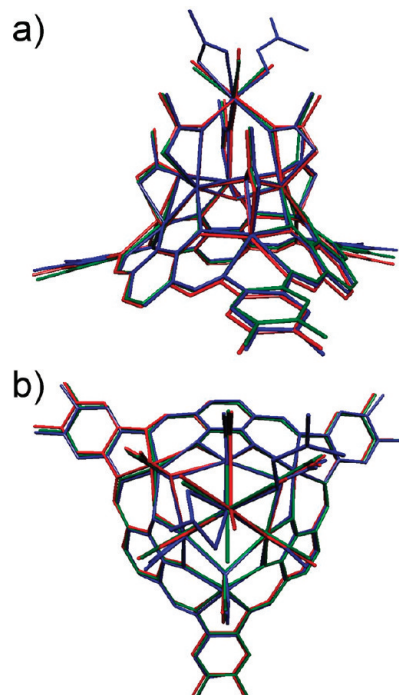


Figure 5. Overlay of geometry-optimized (at ZORA/TZP level) metallocavitand **2e** (red), solid-state structure of **2a** (green), and solid-state structure of **2b** (blue). (a) Side-on view. (b) Top-down view.

performed using the D95V(d,p) basis set and hybrid PB1PBE or B98 xc functionals. To account for relativistic contributions explicitly, and not by means of atom pseudopotentials, further DFT computations were performed at the ZORA level of theory using a TZV Slater functions basis set and pure PBE xc functional. The computed Hessian matrix at different levels of theory did not show any negative eigenvalues qualifying the C₁ point group symmetry structure as a true minimum. Attempts to impose a C_s point group symmetry to the structure of Chart 3b with the aim to reduce the computational effort led to a Hessian matrix with negative eigenvalues associated with the rotation of methyl groups on A and B acetate ligands. The optimized structure at the ZORA TZV/PBE level of theory depicted in Figure 5 is in close agreement with the solid-state structures of **2a** and **2b** and with the other DFT computations as well.

Under all computational conditions explored, the most stable metallocavitand has a μ_3 -hydroxo ligand bridging cadmium ions 4–6 (Chart 2) with an O–H bond pointing directly into the center of the cavity as illustrated in Figure 6. This conformation leaves a W-shaped hydrogen-bonding network between two aqua and one hydroxo ligand coordinated to the cluster capping Cd⁷ characterized by a BSSE corrected interaction energy of the two water molecules with the cluster amounting to $-118.5 \text{ kJ mol}^{-1}$.

A water molecule inside the cavity hydrogen bonding to the μ_3 -oxo ligand does not prevent the rearrangement of the cluster to a μ_4 -oxo species. This indicates that the μ_3 oxygen atom in the field of the four 4–7 Cd atoms has a strong tendency to assume a tetrahedral coordination with “sp³” hybridization and that only a strong interaction with a proton can overcome the alternative interaction with the capping Cd⁷ ion.

The favored μ_3 -OH ligand configuration provides a hydrogen-bonding site inside the already Lewis acidic cavity of metallocavitands **2a–d**, similar to the tantalum boronate metallo-

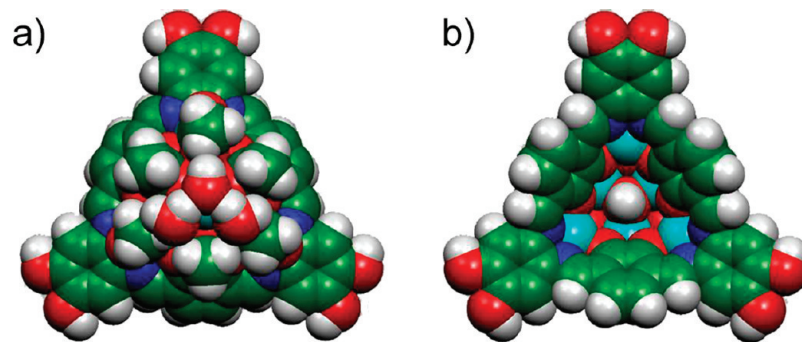


Figure 6. Space filling representations of model metallocavitand **2e** from ZORA/TZP DFT optimization. (a) Top-down view highlighting the W-shaped hydrogen-bonding network of one hydroxo and two aqua ligands facially coordinated to Cd⁷ (Chart 2). (b) Bottom-up view of the cavity with a central $\mu_3\text{-OH}$ ligand bridging Cd^{4–6}. (C = green, H = white, N = blue, O = red, Cd = cyan)

cavitands reported by Fontaine.⁵⁷ The DFT computations show that inside the cavity the μ_3 -hydroxo ligand may hydrogen bond with a water molecule or the carbonyl oxygen of an encapsulated DMF. At the 3-21g/SDD/PBE and D95 V(d,p)/SDD/B98 levels of theory the OH \cdots O distance between the hydrogen atom of the μ_3 -OH and the carbonyl oxygen of the DMF molecule is 1.78 and 1.81 Å, respectively. Taking into account the BSSE correction by CP, the interaction energy of the DMF molecule hydrogen bonded with **2e** by means of the μ_3 -OH at the two levels of theory is –42.05 and –30.59 kJ mol^{–1}, respectively.

A space-filling model suggests that up to three DMF molecules will fit inside the cavity of monomeric metallocavitand **2e**. Energy minimization was performed for metallocavitand **2e** containing one, two, and three DMF molecules in its cavity to determine the optimal occupancy. Four possible DMF-cavity interactions were computed: (1) one DMF molecule H-bonded to the μ_3 -OH ligand; (2) one DMF molecule coordinated to Cd; (3) two DMF molecules each coordinated to Cd; and (4) three DMF molecules all coordinated to Cd atoms. The (DMF)₂ \subset **2e** energy minimization revealed that the situation where each DMF guest molecule is coordinated to cadmium is energetically favored over the case where one DMF is coordinated and one DMF is H-bonded to the μ_3 -OH ligand. In the tri-DMF case there is only sufficient space for each DMF if all are Cd-coordinated and none is H-bonded. The deformation energy⁵⁸ of the metallocavitand and the DMF-cavity corrected BSSE interaction energy were both computed in the gas phase at the D95V(d,p)/SDD/B98 level of theory and gave net interaction energies for scenarios 1–4 of –30.59, –24.10, –24.69, and –30.54 kJ mol^{–1}, respectively. From these values we conclude the cavity of a monomeric metallocavitand in DMF is occupied by one DMF H-bonding to the μ_3 -OH ligand and a few DMF molecules solvating the metallocavitand–DMF complex.⁵⁹ The tri-DMF occupied cavity is next lowest in energy followed by di- and mono- coordinated DMF configurations. Although these calculations do not include the solvation energy, they nicely complement the experimentally determined thermodynamic and kinetic parameters of dimerization and

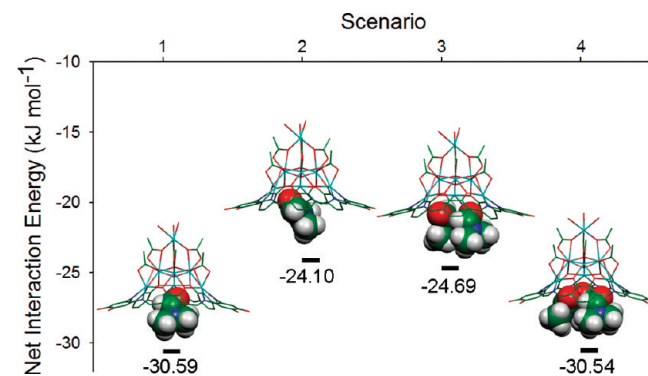


Figure 7. Relative energies of calculated structures for scenario (1) one DMF molecule H-bonded to the μ_3 -OH ligand; (2) one DMF molecule coordinated to a Cd ion; (3) two DMF molecules both coordinated to Cd ions; and (4) three DMF molecules all coordinated to Cd ions.

ligand exchange discussed later in the text. Figure 7 shows the relative energies of the computed structure of **2e** with one, two, or three DMF molecules in the bowl.

Metallocavitand Capsules in Solution: Thermodynamics. Significant resonance broadening, characteristic of a dynamic process on the NMR time scale, was observed in the ¹H NMR spectrum of metallocavitand **2a** in DMF-*d*₇ at room temperature. Coalescence of the resonances assigned to the imine CH, the OCH₂, the OCH₂CH₃, and both aromatic CH protons occurred upon warming from –26 to 47 °C (Figure 8 and SI Figure 2). Integrals of the separated resonances exhibit concentration dependence allowing us to assign them to monomer or dimer. Dimerization constants were calculated (270 ± 10 L mol^{–1} at 25 °C) and a van't Hoff plot was constructed that gave $\Delta H = 19 \pm 1$ kJ mol^{–1} and $\Delta S = 110 \pm 2$ J mol^{–1} K^{–1}.¹⁹ We attribute this entropy-driven and enthalpy-opposed process to expulsion of solvent from the monomer's cavity upon dimerization as shown in Scheme 1.⁶⁰

We expanded our dimerization study to include benzene-*d*₆, toluene-*d*₈, and *p*-xylene-*d*₁₀ by utilizing the enhanced solubility of octyloxy substituted metallocavitand **2d** in nonpolar solvents. In these solvents the rate of monomer–dimer exchange is significantly faster than for **2a** in DMF-*d*₇ and resonances assigned to monomer and dimer cannot be discerned by ¹H NMR spectroscopy even after chilling **2d** in toluene-*d*₈ to –25 °C. Monitoring the imine chemical shift over a series of variable-

(57) (a) Garon, C. N.; Gorelsky, S. I.; Sigouin, O.; Woo, T. K.; Fontaine, F.-G. *Inorg. Chem.* **2009**, *48*, 1699–1710. (b) Sigouin, O.; Garon, C. N.; Delaunais, G.; Yin, X.; Woo, T. K.; Decken, A.; Fontaine, F.-G. *Angew. Chem., Int. Ed.* **2007**, *46*, 4979–4982.

(58) (a) Purcell, K. F.; Kotz, J. C. *Inorganic Chemistry*; Holt Saunders: Philadelphia, 1977; pp 225–226; (b) Ziegler, T. In *Metal-Ligand Interactions: From Atoms, to Clusters, to Surfaces*; Salahub, D. R., Russo, N., Eds.; NATO ASI Series 378; Kluwer Academic Publishers: Amsterdam, 1992, p 367, and references therein.

(59) Considering the solvation of free DMF, scenario 1 is stabilized relative to scenario 4.

(60) (a) Kang, J.; Rebek, J., Jr. *Nature* **1996**, *382*, 239–241. (b) Cram, D. J.; Choi, H. J.; Bryant, J. A.; Knobler, C. B. *J. Am. Chem. Soc.* **1992**, *114*, 7748–7765.

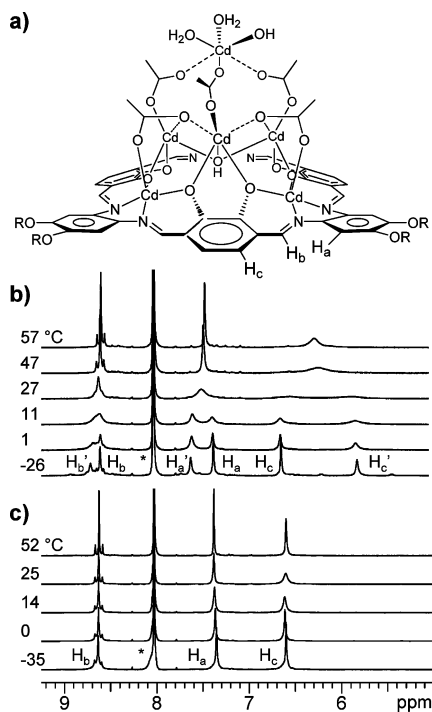
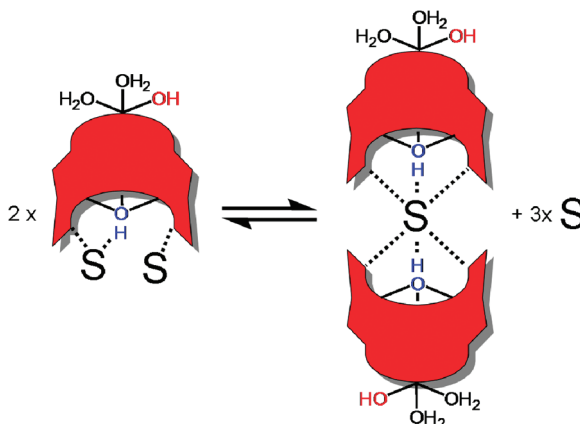


Figure 8. Variable temperature ^1H NMR spectra in $\text{DMF}-d_7$ (400 MHz). (a) Protons H_{a-c} are assigned to the imine and aromatic resonances of metallocavatand **2**, primes ('') belong to the dimer. (b) Dimerization of **2a** results in coalescence of each resonance as the temperature is increased from -26 to $+57\text{ }^\circ\text{C}$. (c) No dimerization is observed for **2b** at low temperature. The DMF resonance, calibrated to 8.03 ppm , is indicated with an *.

Scheme 1. Model for Entropy-Driven Dimerization of Metallocavatands, Rationalized by Solvent Expulsion in the Monomer-Dimer Equilibrium^a



^a S = generic solvent molecules. Multiple solvent molecules interact with the cavity through H-bonds, Cd-coordination, and/or van der Waals interactions (represented by dashed lines).

temperature variable-concentration (VTVC) ^1H NMR spectroscopic experiments allowed us to calculate association constants and thermodynamic parameters of **2d** in these solvents.⁶¹ Thermodynamic data are summarized in Table 1; in all cases, dimerization is an entropy-driven process.¹⁹

Since metallocavatand dimerization involves solvent encapsulation, we first turned to the “55% rule” for molecular recognition, developed by Mecozzi and Rebek, to rationalize our thermodynamic parameters.⁴⁶ The empirical model predicts

(61) Horman, I.; Dreux, B. *Helv. Chim. Acta* **1984**, *67*, 754–764.

Table 1. Thermodynamics of Dimerization for Metallocavatands **2a** and **2d** in Various Deuterated Solvents^a

	2a	2d		
solvent	DMF	benzene	toluene	<i>p</i> -xylene
K_{dim} (L mol^{-1}) ^b	270 ± 10	800 ± 100	1500 ± 400	1000 ± 300
ΔH (kJ mol $^{-1}$)	19 ± 1	-7 ± 5	1 ± 4	11 ± 8
ΔS (J mol $^{-1}$ K $^{-1}$)	110 ± 2	32 ± 14	64 ± 14	94 ± 24
$V_{\text{guest}}/V_{\text{host}}$ %	40/80 ^c	46	54	63

^a The packing coefficient is also included as a percentage.⁴⁶

^b Calculated at $25\text{ }^\circ\text{C}$ from van't Hoff plots. ^c Calculated for single and double occupancy.

that optimal guest recognition occurs when the guest occupies $55 \pm 9\%$ of the host's void space. In our system, each metallocavatand capsule has a void space of $215\text{ }\text{\AA}^3$, and packing coefficients for DMF, benzene, toluene, and *p*-xylene are 0.40 (0.80 for 2 DMFs), 0.46, 0.54, and 0.63, respectively.⁶² Dimerization constants for **2** follow the 55% rule quite well, with the highest being in toluene followed by *p*-xylene, benzene, and finally DMF.

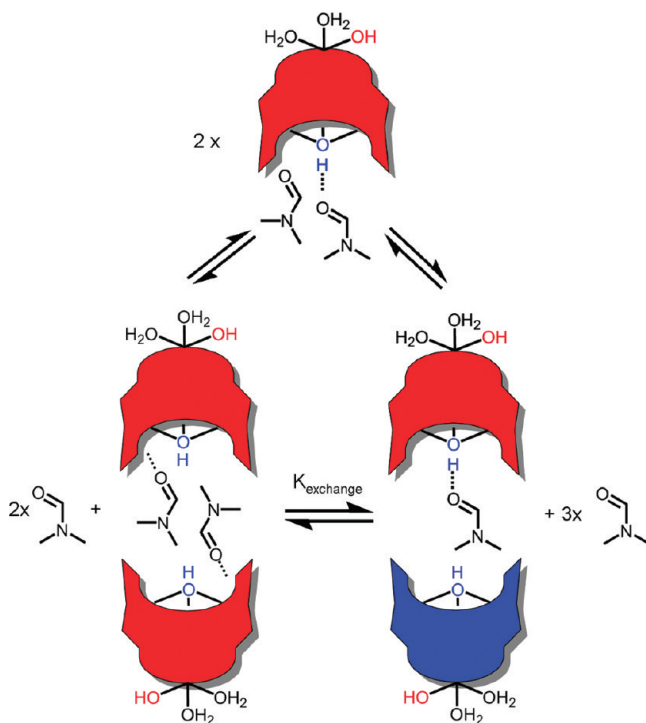
In our entropy-driven system, the 55% rule is not expected to exactly apply since solvent release from the monomer is probably the most important criterion for dimerization: the more restricted that solvent is in the cavity of the monomer, the greater the entropy increase when it is released during dimerization. Aromatic solvents (e.g., benzene, toluene, and xylenes) or Lewis bases (DMF) that can participate in strong host–guest interactions with the cavity of monomeric **2** facilitate dimerization, whereas other solvents that only interact weakly with the monomer (e.g., CH_2Cl_2 and CHCl_3) do not lead to dimerization despite packing coefficients similar to that for DMF.

Dimerization is an enthalpy-opposed process in all solvents except benzene-*d*₆, suggesting the face-to-face van der Waals interactions between metallocavatands in the dimeric state are negligible relative to solvent-cavity interactions. Since the cavity of each monomeric metallocavatand is solvated by multiple guests, most of these cavity-guest interactions must be eradicated upon dimerization to accommodate the volume restraints imposed by capsule formation. The large positive enthalpy contribution for DMF results from cleavage of $\mu_3\text{-OH}\cdots\text{O}_{\text{DMF}}$ hydrogen bonds upon dimerization; however, the enthalpy differences between aromatic solvents are harder to rationalize. Less favorable packing coefficients and perhaps more favorable cavity-methyl group interactions may explain the enthalpy increase from benzene to *p*-xylene. In benzene, capsule assembly is spontaneous regardless of temperature suggesting the solvent-cavity interactions in the monomeric state are quite weak or the smaller guest allows for closer/stronger contacts between metallocavatands in the dimer.

Regardless of solvent type, entropy-driven dimerization is observed due to expulsion of solvent from the monomer's cavity upon capsule formation. Dimerization of **2a** in DMF shows the highest entropy contribution followed by **2d** in *p*-xylene, toluene, and finally benzene. This trend may be attributed to stronger cavity-DMF interactions binding DMF tighter than cavity-aromatic solvent interactions. Steric effects may be responsible for the reduced entropic contribution from *p*-xylene to benzene; bulkier solvent has less “wiggle” room inside the monomer's cavity and therefore gains more entropy upon expulsion from the cavity.

(62) The capsule void space was calculated with PLATON,⁴⁵ and solvent volumes were calculated with SPARTAN 04, Wavefunction Inc. 2004, Irvine, CA. USA.

Scheme 2. Equilibria between DMF \subset **2a**, (DMF)₂ \subset **2a·2a**, and DMF \subset **2a·2a^a**



^a Encapsulated DMF is not able to invert making the capsule halves unsymmetrical in DMF \subset **2a·2a** (red and blue).

We anticipated dimerization of metallocavatand **2b** in DMF-_d₇ to proceed similarly to **2a**; however, we observed no evidence for dimerization in the low temperature ¹H NMR spectrum (Figure 8c). Aromatic and imine resonances of **2b** exhibit a slight sharpening as the temperature decreases and their chemical shift is static below 14 °C. Despite packing into a dimer in the solid state, rapid spinning/tumbling of the bulky neopentyloxy chains prohibits dimerization in solution.

Capsule Occupancy and the μ_3 -OH Proton NMR Resonance. An incongruity arises between our solution-state 55% rule analysis and the solid-state structures of **2a** and **2b**: in the solid state two DMF molecules are found in each capsule. The resulting exceptionally high packing coefficient, 0.80, may be explained by metal coordination and weak hydrogen-bond synergy between host and guests. Complementary interactions between host and guest result in enhanced packing coefficients, effectively “increasing” the cavity volume.⁶³ Low temperature ¹H NMR spectroscopy in DMF-_d₇ confirmed doubly occupied capsules, (DMF)₂ \subset **2a·2a**, are prominent in solution; however, a small fraction of capsules are singly occupied, DMF \subset **2a·2a**. We speculate that the capsule (DMF)₂ \subset **2a·2a** may be sufficiently dynamic to expel one guest DMF, giving DMF \subset **2a·2a** + DMF, without fully dissociating as shown in Scheme 2.

Perturbation of a host’s symmetry due to guest orientation is frequently observed by ¹H NMR spectroscopy in host–guest systems.⁶⁴ Thorough examination of the ¹H NMR spectrum of **2a** obtained at -24 °C in DMF-_d₇ reveals three different sets of resonances that are highlighted in Figure 9. Resonances found at 8.6, 7.4, and 6.6 ppm confirm monomer **2a** has *C*₃ rotational

symmetry and suggest that guest DMF molecules are labile or dynamic on the NMR time scale. Two explanations arise for the *D*_{3d} symmetry observed for the dominant **2a** dimer resonances found at 8.7, 7.6, and 5.8 ppm: (1) one DMF molecule is encapsulated that may rotate about the *C*₃ axis of the capsule and invert freely around an axis perpendicular to the *C*₃ axis or (2) two DMF molecules are encapsulated and rotate simultaneously about the axis of the capsule without inversion. In both cases, the capsule halves remain equivalent and *C*₃ rotational symmetry is maintained. The latter explanation is supported by solid-state analyses that revealed two DMF molecules inside each capsule and steric constraints inside the capsule suggest inversion is significantly hindered.

We expect the simultaneous rotation of both encapsulated DMF molecules requires some expansion of the capsule and/or breathing of the cavity walls. In fact the very low frequency vibration modes^{65,66} $\nu_1 = 18\text{ cm}^{-1}$, $\nu_2 = 20\text{ cm}^{-1}$, and $\nu_4 = 25\text{ cm}^{-1}$ calculated at the D95V(d,p)/SDD/B98 level of theory are related to the breathing motion of the macrocyclic ligand suggesting that the energy requirement for this type of distortion is very small. It is likely that the conformational flexibility that allows for rotation may also lead to the escape of one encapsulated DMF yielding the unsymmetrical capsule DMF \subset **2a·2a**.⁶⁷

Resonances of DMF \subset **2a·2a** are evenly distributed around resonances of (DMF)₂ \subset **2a·2a** and integration of the ¹H NMR spectrum obtained at -24 °C gives a global equilibrium constant between (DMF)₂ \subset **2a·2a** and DMF \subset **2a·2a** of $K_{\text{exchange}} = 0.32 \pm 0.06$. This equilibrium constant also accounts for dimerization of monomers yielding the unsymmetrical capsule DMF \subset **2a·2a**.⁶⁸ Despite dimerization being entropy driven, the entropy gained by expelling all but one DMF molecule is counteracted by the enthalpy loss associated with cleaving the hydrogen and coordination bonds between metallocavatand and DMF, making the capsule (DMF)₂ \subset **2a·2a** thermodynamically favored over DMF \subset **2a·2a**.

Besides observation of unsymmetrical capsules in low temperature ¹H NMR spectra, the suppression of dimerization and guest exchange kinetics allowed us to resolve the resonance of the proton of the μ_3 -OH ligand bridging cadmium ions 4–6 (Chart 2). At 15 °C a low-intensity, broad resonance emerged from the baseline at 2.35 ppm and sharpened considerably upon chilling the sample to -24 °C. We initially believed it to be an impurity; however, the resonance, depicted in Figure 10, has an exceptionally diagnostic splitting pattern that was successfully simulated as two-bond coupling of the μ_3 -OH proton to three chemically equivalent cadmium ions. Both ¹¹¹Cd and ¹¹³Cd are roughly 12% abundant, have a spin of 1/2, and couple to μ_3 -OH proton with a *J* = 13 Hz. The simulation was performed

(64) Recent review: (a) Rebek, J., Jr. *Angew. Chem., Int. Ed.* **2005**, *44*, 2068–2078. Recent references: (b) Power, N. P.; Dalgarno, S. J.; Atwood, J. L. *Angew. Chem., Int. Ed.* **2007**, *46*, 8601–8604. (c) Kobayashi, K.; Kitagawa, R.; Yamada, Y.; Yamanaka, M.; Suematsu, T.; Sei, Y.; Yamaguchi, K. *J. Org. Chem.* **2007**, *72*, 3242–3246. (d) Haino, T.; Kobayashi, M.; Chikaraishi, M.; Fukazawa, Y. *Chem. Commun.* **2005**, 2321–2323.

(65) See SI for a plot of low frequency modes.

(66) $\nu_3 = 24\text{ cm}^{-1}$ is related to the torsion of the whole Cd-acetate ligand system with respect to the macrocyclic system.

(67) Reviews on guest exchange in capsules: (a) Pluth, M. D.; Raymond, K. N. *Chem. Soc. Rev.* **2007**, *36*, 161–171. (b) Palmer, L. C.; Rebek, J., Jr. *Org. Biomol. Chem.* **2004**, *2*, 3051–3059. (c) Hof, F.; Craig, S. L.; Nuckolls, C.; Rebek, J., Jr. *Angew. Chem., Int. Ed.* **2002**, *41*, 1488–1508.

(68) The low intensity of these resonances prevented a full thermodynamic analysis.

(63) Fairchild, R. M.; Holman, K. T. *J. Am. Chem. Soc.* **2005**, *127*, 16364–16365.

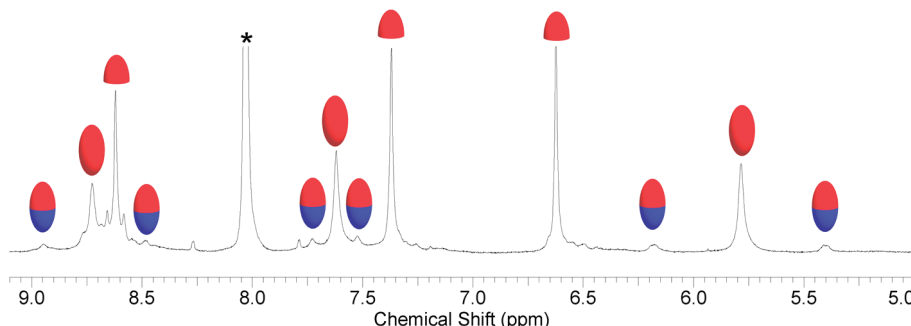


Figure 9. Downfield region in the ^1H NMR spectrum of metallocavatand **2a** at -24°C (400 MHz, $\text{DMF}-d_7$). Three sets of resonances belonging to $\text{DMF} \subset 2\mathbf{a}$, $(\text{DMF})_2 \subset 2\mathbf{a} \cdot 2\mathbf{a}$, and $\text{DMF} \subset 2\mathbf{a} \cdot 2\mathbf{a}$ are observed and labeled with a half capsule (red), whole capsule (red), and unsymmetrical whole capsule (red and blue), respectively. Resonances of the unsymmetrical capsule halves in $\text{DMF} \subset 2\mathbf{a} \cdot 2\mathbf{a}$ are perfectly distributed around the $(\text{DMF})_2 \subset 2\mathbf{a} \cdot 2\mathbf{a}$ resonances. The DMF resonance, calibrated to 8.03 ppm, is indicated with an *.

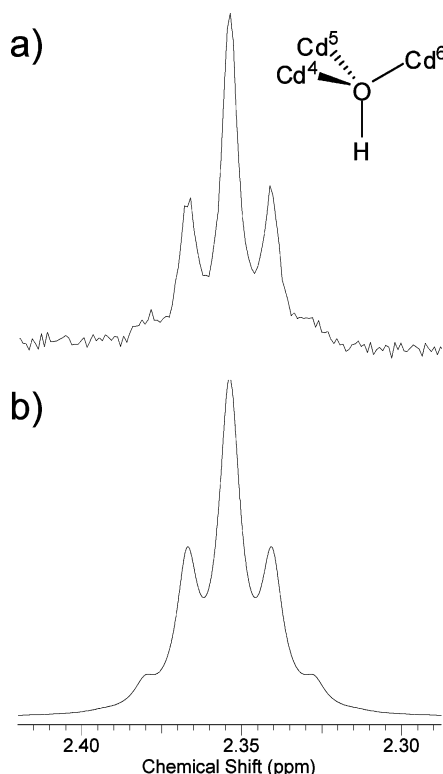


Figure 10. (a) ^1H NMR spectrum for the $\mu_3\text{-OH}$ proton resonance belonging to monomeric metallocavatand **2a** ($\text{DMF}-d_7$, -24°C , 400 MHz). Inset depicts the environment that results in the observed spin system. Cadmium labels are from Chart 2. (b) Simulation of the spin system with $J_{\text{H-Cd}} = 13$ Hz and 4 Hz of line broadening.

with all ten possible permutations, a J value of 13 Hz, and 4 Hz of line broadening.⁶⁹ Integration of the $\mu_3\text{-OH}$ proton resonance at 2.35 ppm shows this particular resonance belongs to the monomer and another resonance found at 2.51 ppm with the same splitting pattern belongs to the $\mu_3\text{-OH}$ proton resonance of the symmetric capsule, $(\text{DMF})_2 \subset 2\mathbf{a} \cdot 2\mathbf{a}$ (integral ratio 1.0/0.7, respectively).⁷⁰ Both $\mu_3\text{-OH}$ proton resonances are lost upon addition of D_2O , confirming a proton exchange pathway is

active. Depressed guest exchange, dimerization, and/or H-bonding rates may all be responsible for the sharpening of these resonances at low temperature. This unequivocal piece of evidence eliminates any remaining doubt about the proton assignment. We believe this is the first report of $^2J(^{111/113}\text{Cd}/^1\text{H})$ coupling in a cadmium-hydroxo compound. In most other complexes, the NMR spectra are obtained in water or in other solvents where the proton can rapidly exchange. The sheltered environment of the metallocavatands prevents rapid exchange and offers a unique opportunity to observe this coupling.

Metallocavatand Capsules in Solution: Kinetics. Although metallocavatand dimerization is a complex event, involving multiple guest–cavity, cavity–cavity, and guest–guest interactions, some mechanistic information may be gained from kinetic measurements. Since dimerization of **2a** in $\text{DMF}-d_7$ occurs on the NMR time scale, we chose to study this system over **2d** in aromatic solvents where very rapid exchange is observed. Coalescence temperatures of the resonances assigned to the imine, downfield aromatic, upfield aromatic, methylene, and methyl protons of **2a** were recorded in $\text{DMF}-d_7$ from variable temperature ^1H NMR spectroscopic experiments and then fit to an unequally populated two-site exchange model.⁷¹ Rates were calculated and an Eyring plot was constructed (SI Figure 3) giving a k_{dim} of 170 s^{-1} at 25°C , $\Delta H^\ddagger = 69 \pm 13\text{ kJ mol}^{-1}$, and $\Delta S^\ddagger = -410 \pm 60\text{ J mol}^{-1}\text{ K}^{-1}$. A large negative entropy contribution indicates the mechanism is associative in nature and a high degree of order must be imparted upon the system. As the temperature drops below -26°C , the dimerization rate approaches zero and a static mixture of monomer and dimer results. The accelerated dimerization rate qualitatively observed for **2d** in nonpolar organic solvents relative to **2a** in $\text{DMF}-d_7$ suggests the mechanism of dimerization may be different when a coordinating solvent (e.g., DMF) is present.

Cadmium Cluster Dynamics: A Molecular Beehive. Besides dimerization, careful inspection of the acetate resonances of **2a** and **2b** in the ^1H NMR spectra obtained at different temperatures revealed more dynamic behavior. In $\text{DMF}-d_7$, at room temperature, the acetate, aqua, and capping hydroxo ligands are rapidly exchanging or “buzzing around” the cadmium cluster. This rapid exchange is manifested in a single broad resonance located around 2 ppm and assigned by integration of the proton resonances to both acetate environments and the capping aqua/

(69) Simulated permutations: $^1\text{H}^{112}\text{Cd}^{112}\text{Cd}^{112}\text{Cd}$ singlet 0.4217 probability, $^1\text{H}^{112}\text{Cd}^{112}\text{Cd}^{111}\text{Cd}$ doublet 0.2151 probability, $^1\text{H}^{112}\text{Cd}^{112}\text{Cd}^{113}\text{Cd}$ doublet 0.2068 probability, $^1\text{H}^{112}\text{Cd}^{111}\text{Cd}^{111}\text{Cd}$ triplet 0.0366 probability, $^1\text{H}^{112}\text{Cd}^{113}\text{Cd}^{113}\text{Cd}$ triplet 0.0338 probability, $^1\text{H}^{112}\text{Cd}^{111}\text{Cd}^{113}\text{Cd}$ triplet 0.0703 probability, $^1\text{H}^{111}\text{Cd}^{113}\text{Cd}^{113}\text{Cd}$ quartet 0.0057 probability, $^1\text{H}^{113}\text{Cd}^{111}\text{Cd}^{111}\text{Cd}$ quartet 0.0060 probability, $^1\text{H}^{111}\text{Cd}^{111}\text{Cd}^{111}\text{Cd}$ quartet 0.0021 probability, $^1\text{H}^{113}\text{Cd}^{113}\text{Cd}^{113}\text{Cd}$ quartet 0.0018 probability.

(70) Low concentration of the unsymmetrical capsule, $\text{DMF} \subset 2\mathbf{a} \cdot 2\mathbf{a}$, prevented us from locating the corresponding $\mu_3\text{-OH}$ proton resonance in the ^1H NMR spectrum.

(71) Pons, M.; Millet, O. *Prog. Nucl. Magn. Reson. Spectrosc.* **2001**, 38, 267–324.

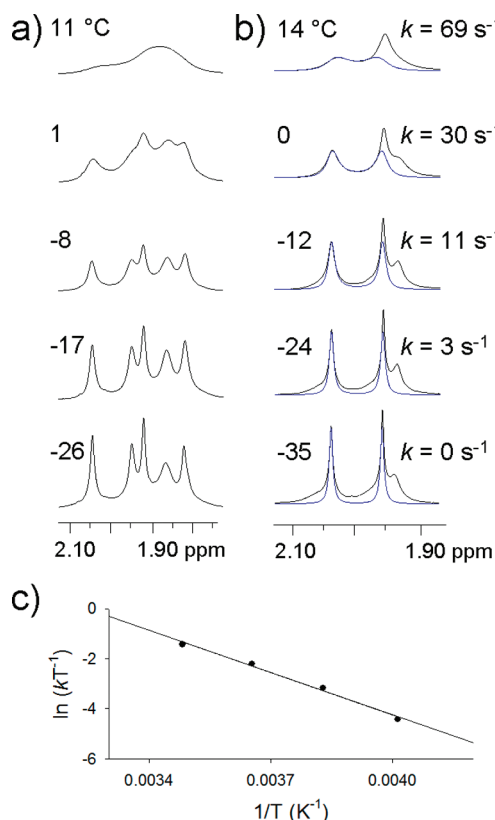


Figure 11. Dynamic ligand exchange in $DMF-d_7$ is confirmed by coalescence of the acetate resonances in variable temperature 1H NMR spectra. (a) Upon cooling a solution of metallocavatand **2a**, two sets of two acetate resonances emerge with each set corresponding to monomer or dimer. (b) In the absence of dimerization, only a single set of two acetate resonances is observed for metallocavatand **2b**. Rates of exchange were calculated from the simulated resonances shown in blue. In each spectrum, the additional broad resonance is assigned to the coordinated aqua/hydroxo capping ligands. (c) Eyring plot of acetate exchange for metallocavatand **2b** ($r^2 = 0.992$).

hydroxo ligands. Although the rate of Cd-aqua/hydroxo exchange is known to be very fast ($>10^6\text{ s}^{-1}$),⁷² we were able to slow the rate of acetate exchange to the NMR time scale by chilling the sample.

At low temperature, the broad resonance at 2 ppm separates into two acetate resonances at 2.05 and 1.95 ppm and one broad aqua/hydroxo proton resonance at 1.94 ppm belonging to monomeric metallocavatand **2b**. These same monomer resonances are found in the low temperature spectrum of **2a** along with two acetate resonances belonging to dimers of **2a** found at 1.93 and 1.86 ppm. Figure 11 shows coalescence of the acetate region in variable temperature 1H NMR spectra. The acetate lability is highly solvent dependent; in $CDCl_3$, distinct type-A and B acetate resonances (Chart 2) are evident in the 1H NMR spectra of metallocavatands **2c** and **2d** at room temperature suggesting exchange is very slow or nonexistent. When $DMF-d_7$ is added to a solution of **2d** in $CDCl_3$, coalescence of type-A and B acetate resonances is observed, linking DMF to the mechanism of acetate exchange.

In the case of complex **2b**, where the bulky neopentyloxy substituents prevent dimerization, the acetate region of the 1H NMR spectrum was easily simulated providing quantitative

kinetic information about the rate of acetate exchange.⁷³ From the Eyring plot shown in Figure 11c, $k_{\text{exchange}} = 160\text{ s}^{-1}$ at 25 °C, $\Delta H^\ddagger = 47 \pm 13\text{ kJ mol}^{-1}$, and $\Delta S^\ddagger = -490 \pm 120\text{ J mol}^{-1}\text{ K}^{-1}$, respectively. Within experimental error these values are intriguingly similar to those obtained for dimerization of **2a** in $DMF-d_7$. The only reasonable explanation for this kinetic congruity is that both mechanisms share a common rate-determining step.

Transition state solvation requires a high degree of order resulting in large negative entropy terms similar to those observed for both acetate exchange and dimerization of our metallocavatands. Intuitively, solvent-cavity interactions are involved in the mechanism of dimerization and may be invoked to explain the $\Delta S^\ddagger = -410 \pm 60\text{ J mol}^{-1}\text{ K}^{-1}$ observed for dimerization of **2a**; it is less obvious, however, how cavity solvation plays a role in the mechanism of acetate exchange. We propose these two processes share a rate-determining transition state that involves the coordination of two DMF molecules to available cadmium centers inside the cavity of monomeric metallocavatands as outlined in Figure 12. To accommodate two DMF molecules inside the cavity, the $\mu_3\text{-OH} \cdots O_{DMF}$ hydrogen bond with one DMF must be broken as the DMF forms a bond to one of the N_2O_2 chelated cadmium ions 1–3 (Chart 2), and a second nearby solvating DMF molecule must bond to a cadmium ion in the cavity contributing to the negative entropy. Cleavage of the stronger hydrogen bond and formation of the weaker coordination bonds are responsible for the positive enthalpy observed for this intermediate, as calculated earlier (Figure 7). After this rate-determining step, a third molecule of DMF may enter the bowl and coordinate to the last vacant site on cadmium, forming a more stable intermediate. The computed model (DFT) of this intermediate shows there is sufficient space inside the cavity for a third DMF guest molecule to coordinate to a cadmium ion only if none of the DMF molecules is simultaneously hydrogen bonding with the $\mu_3\text{-OH}$ ligand (Figure 13). After formation of the tri-DMF intermediate, the mechanisms of acetate exchange and dimerization diverge.

Coordination of a third DMF molecule saturates all of the N_2O_2 chelated cadmium ions (1–3, Chart 2) and destabilizes each type-A OAc–Cd bond trans to the DMF ligands. When three DMF molecules are coordinated inside the cavity, the absence of a $\mu_3\text{-OH} \cdots O_{DMF}$ hydrogen bond localizes all of the carbonyl (DMF) electron density on cadmium ions 1–3, lowering the activation barrier to OAc–Cd bond scission. Indeed, the calculations of the complex with three coordinated DMF molecules in the bowl shows that the Cd–OAc bonds are lengthened by as much as $\sim 0.1\text{ \AA}$. Cleavage of the Cd–OAc bonds and subsequent type-A to B acetate exchange must happen rapidly compared to the initial association of a second DMF inside the cavity. DMF coordination is essential to promote acetate exchange as exchange is not observed in noncoordinating solvents such as $CDCl_3$ until small quantities of DMF are introduced.

Acetate exchange also has long-range effects on the rigidity of the cavity. Broadening of the proton resonance of the catechol unit pointing out of the cavity is observed at room temperature by 1H NMR spectroscopy of metallocavatand **2b** (H_c in Figure 8c). Upon cooling the sample, the proton resonances of the catechol (CH) and acetate sharpened simultaneously suggesting

(72) Tobe, M. L., Burgess, J., Eds.; *Inorganic Reaction Mechanisms*; Addison Wesley Longman Inc.: New York, 1999.

(73) Marat, K. *Spinworks, ver. 3.0*; University of Manitoba: Winnipeg, Canada, 2008.

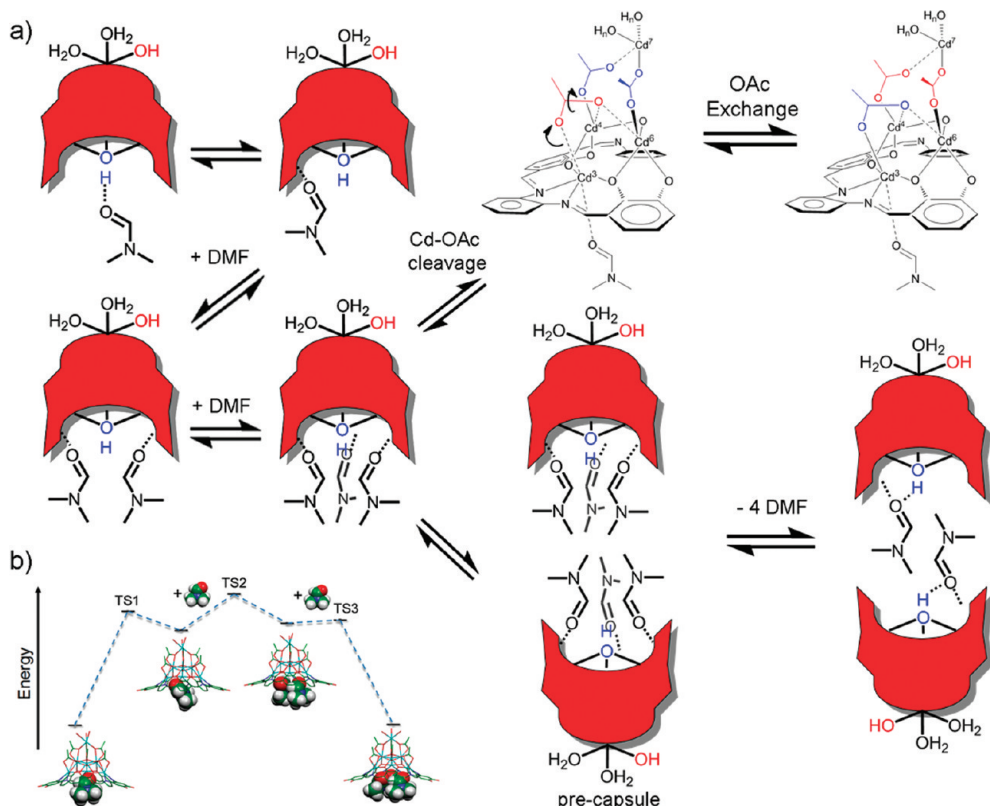


Figure 12. (a) Proposed mechanism for formation of the tri-DMF intermediate that initiates both acetate exchange (top right) and dimerization (bottom right). The rate-determining step involves formation of two Cd–O (DMF) coordination bonds after the $\mu_3\text{-OH}\cdots\text{O}_{\text{DMF}}$ hydrogen bond is broken. In the top right, rapid cleavage of the Cd–OAc bond is promoted by guest DMF molecules trans to the acetate ligands and followed by exchange between type-A and B acetates, depicted in red and blue, respectively (much of the cluster has been omitted for clarity). In the bottom right, dimerization proceeds first by formation of a precapsule assembly followed by loss of coordinated DMF and fast dimerization of the unsaturated metallocavitands. (b) Energy profile diagram leading to the tri-DMF coordinated intermediate.

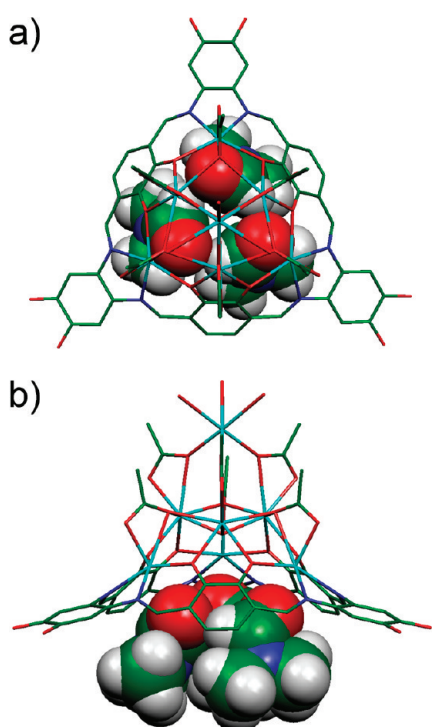


Figure 13. DFT (D95V(d,p)/SDD/B98) energy-minimized structure of intermediate where all three DMF guest molecules are coordinated to cadmium ions 1–3 (Chart 2) in **2e** and none is interacting with the $\mu_3\text{-OH}$ ligand. (a) Top-down. (b) Side-on.

the metallocavitand “breathes” when the acetates are labile, but as their exchange is slowed, the cavity rigidifies.

The tri-DMF reactive intermediate is actually more compact than the ground state hydrogen-bonded DMF assembly and will allow for two metallocavitands to enter in close proximity forming a 6 DMF + 2 metallocavitand precapsule assembly. Expulsion of coordinated DMF from the compact precapsule leads to dimerization yielding a capsule with two encapsulated DMF molecules both coordinated and hydrogen bonded as observed in the solid-state. We hypothesize that competition between DMF guests to form a hydrogen bond with the $\mu_3\text{-OH}$ ligand and subsequent dimerization of the unsaturated metallocavitands proceeds quickly.

Our acetate exchange and dimerization mechanisms fit reasonably well to the experimental and computational evidence. We acknowledge, however, that these events are more intricate than our observations indicate; it is not possible for us to calculate the exact transition state for such an enormous cluster. Nevertheless, from our data, we have shown that the dimerization requires association followed by solvent expulsion from the bowl rather than the other way around and that the rate-determining step involves coordination of the DMF to the metal center inside the bowl.

Guest Dynamics Probed by Solid-State NMR Spectroscopy.

In solution, fast dimerization kinetics hindered our investigation of guests encapsulated in metallocavitands **2a–d**. To overcome this setback, we have conducted solid-state NMR spectroscopic experiments to study guest dynamics in metallocavitand capsules.⁷⁴ Interestingly, we are able to remove one encapsulated

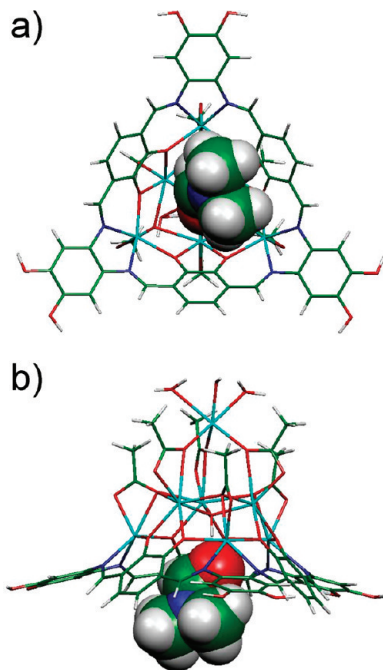


Figure 14. DFT (D95V(d,p)/SDD/B98) energy-minimized geometry of DMF hydrogen bonding inside the cavity of **2e**. (a) Top-down view looking down the 3-fold axis of rotation. (b) Side-on view showing the H-bond. DMF is depicted as space-filling.

DMF molecule after heating capsules of **2a** under vacuum for 48 h as confirmed by ¹H NMR spectroscopy in DMSO-*d*₆. For solid-state ²H NMR spectroscopic investigations, samples of **2a** were recrystallized from DMF-*d*₇ followed by heating under vacuum for 48 h to give capsules of **2a** with one DMF-*d*₇ molecule encapsulated. Figure 14 depicts the DFT-optimized orientation of DMF hydrogen-bonding with the μ_3 -OH ligand inside the cavity.

Solid-state ²H NMR powder lineshapes depend on the interaction between the electric quadrupole moment of the deuterium nucleus and the electric field gradient tensor at the nuclear site. Although the quadrupole moment is invariant, the observed electric field gradient tensor depends on the degree of motional averaging. The ²H NMR lineshapes are therefore very sensitive to and characteristic of both the mechanism and rate of molecular motion.⁷⁵ In the absence of molecular motion, solid-state ²H NMR spectra take on a line shape like that shown in Figure 15a, described by splittings, $\Delta\nu_{xx}$, $\Delta\nu_{yy}$, and $\Delta\nu_{zz}$ and characterized by the quadrupolar coupling constant, $\chi = e^2 Qq/h$ and asymmetry parameter, η , where

$$\Delta\nu_{xx} = (3\chi/4)(1 - \eta)$$

$$\Delta\nu_{yy} = (3\chi/4)(1 + \eta)$$

$$\Delta\nu_{zz} = 3\chi/2$$

$$\eta = (\Delta\nu_{yy} - \Delta\nu_{xx})/\Delta\nu_{zz} \quad 0 \leq \eta \leq 1$$

When a molecular motion occurs at a rate that is fast with respect to the reciprocal of the overall static line width, $\Delta\nu_{zz}$, χ is averaged by the motion, and the line shape is as described above with χ replaced by χ' , the reduced quadrupolar coupling constant defined by the molecular motion. An example of what one would expect for fast methyl group rotation is shown in Figure 15b. When the molecular motion occurs at a rate of the

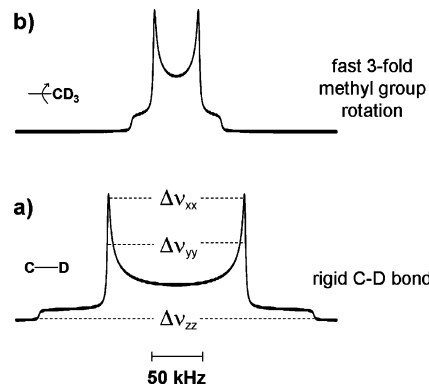


Figure 15. ²H NMR powder lineshapes for (a) a rigid C–D bond and (b) a methyl group rotating at a rate which is fast with respect to the static line width.

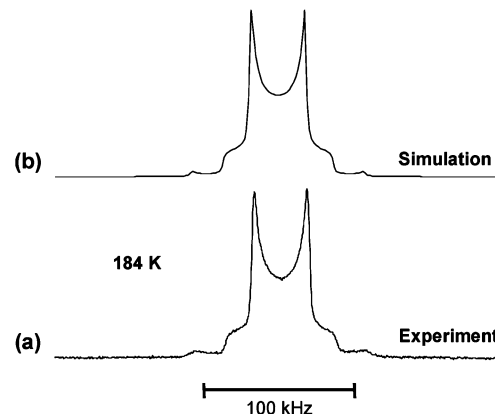


Figure 16. (a) Experimental and (b) simulated solid-state ²H NMR spectra of DMF-*d*₇ trapped in the capsules of **2a** at 184 K. There are two overlapping powder patterns contributing to the spectrum. The more intense contribution is due to the rotating $-\text{CD}_3$ groups and the broader, less intense contribution is due to the amide deuteron.

same order as the reciprocal line width, the line shape is more complicated and very sensitive to the rate of the motion.⁷⁶

The solid state ²H NMR spectrum of DMF-*d*₇ trapped within the cavities of **2a** at 184 K is shown in Figure 16a and simulated in Figure 16b. The spectrum consists of two overlapping powder patterns: one from the methyl deuterons ($\chi' = 49 \pm 2$ kHz, $\eta = 0$, relative intensity = 6) and one from the amide deuteron ($\chi = 155 \pm 4$ kHz, $\eta = 0$, relative intensity = 0.31). The expected intensity ratio of 6:1 is not observed as the T_1 for the amide deuteron is longer than that for the methyl deuterons. The 5 s recycle delay used in the measurement was insufficiently long to allow for full relaxation of the amide deuteron. The quadrupolar coupling constant for the amide deuteron of DMF-*d*₇ has been reported to be between 154 and 181 kHz and those for rigid methyl deuterons between 156 kHz and 167 kHz.⁷⁷ Our observation of $\chi = 155$ kHz for the amide deuteron indicates that the amide C–D bond is essentially rigid and is consistent with the hydrogen bonding we observe.

(74) Some recent examples of guest dynamics studied by solid-state NMR spectroscopy: (a) Chierotti, M. R.; Gobetto, R. *Chem. Commun.* **2008**, 1621–1634. (b) Al bunia, A. R.; Gaeta, C.; Neri, P.; Grassi, A.; Milano, G. *J. Phys. Chem. B* **2006**, 110, 19207–19214.

(75) Wittebort, R. J.; Olejniczak, E. T.; Griffin, R. G. *J. Chem. Phys.* **1987**, 86, 5411–5420.

(76) Greenfield, M. S.; Ronemus, A. D.; Vold, R. L.; Vold, R. R.; Ellis, P. D.; Raidy, T. E. *J. Magn. Reson.* **1987**, 72, 89–107.

(77) Balakrishnan, N. S. *J. Magn. Reson.* **1989**, 83, 233–245.

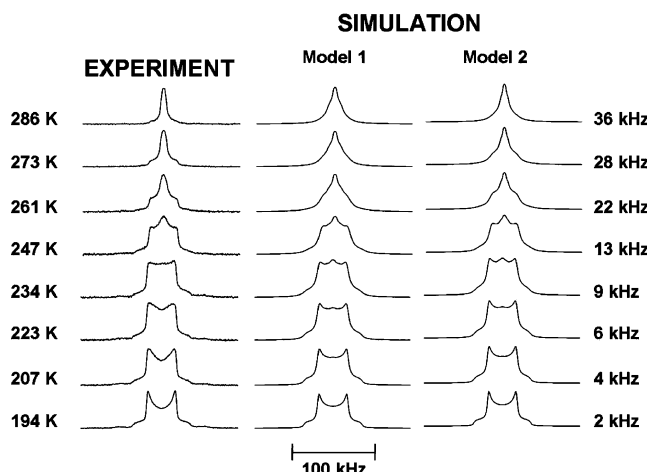


Figure 17. Experimental and simulated solid-state ^2H NMR spectra for DMF- d_7 trapped in the capsules of **2a** measured as a function of temperature. Model 1 is a 3-fold rotation of the $\text{N}-(\text{CD}_3)_2$ moiety about the bisector of the $(\text{CD}_3)-\text{N}-(\text{CD}_3)$ bond angle. Model 2 is an overall 3-fold molecular rotation about an axis defined by our DFT calculations.

The reduced quadrupolar coupling constant of 49 kHz observed for the methyl deuterons is typical for fast 3-fold methyl group rotation⁷⁸ in which case χ' is expected to be $\chi/3 \approx 54$ kHz. The additional reduction of χ' to 49 kHz may be due to an additional small scale librational motion. The ^2H NMR spectra measured as a function of temperature are shown in Figure 17 along with simulations. As the contribution from the amide deuteron is much broader than that for the methyl deuterons and has only a minor contribution to the overall spectrum, it was neglected in the simulations. The changes in line shape observed as a function of temperature indicate that in addition to the fast methyl group rotation, a large scale molecular motion also occurs. Furthermore, since we do not observe two different overlapping powder spectra in a 1:1 ratio for the CD_3 groups, each methyl group must be treated identically by the motion.

The spectra are consistent with an n -fold rotation ($n \geq 3$) of the methyl groups about an axis 60° from each of the $\text{N}-(\text{CD}_3)$ bonds. One model that would explain the spectra (model 1 in Figure 17) is a rotation of the $\text{N}-(\text{CD}_3)_2$ moiety about the bisector of the $(\text{CD}_3)-\text{N}-(\text{CD}_3)$ bond angle. For such a motion, both methyl groups precess on the surface of a cone of half angle 60° . It may be reasonable to assume that $n = 3$, in accordance with the approximate 3-fold symmetry of the void space of the capsule. Our DFT calculations, however, give us reason to believe that this is not the case.

Calculations indicate that the DMF molecule is hydrogen bonded with the $\mu_3\text{-OH}$ ligand inside the capsule and any motion of the DMF molecule is likely to be a rotation about the $\mu_3\text{-OH}\cdots\text{O}_{\text{DMF}}$ hydrogen bond (model 2 in Figure 17). If this axis of rotation is translated such that it passes through the nitrogen atom of the DMF molecule, the methyl groups lie on cones of half an angle 61.2° and 64.6° . These angles are reasonably close to 60° and the effects on the ^2H NMR spectrum resulting from a 3-fold rotation about this axis, in accordance with the approximate 3-fold symmetry of the void space, will be similar to those for a simple 3-fold internal rotation of the $\text{N}-(\text{CD}_3)_2$ moiety about the bisector of the $(\text{CD}_3)-\text{N}-(\text{CD}_3)$ bond angle.

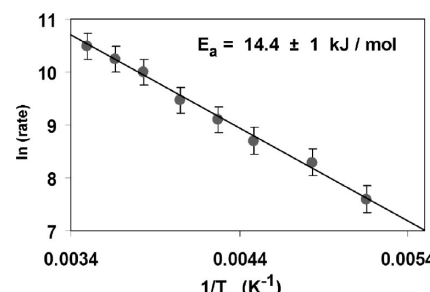


Figure 18. Arrhenius plot for the rotation of DMF- d_7 in the capsules of **2a** ($r^2 = 0.995$).

For model 2 in Figure 17, spectra were simulated independently for each of the methyl groups and the two spectra were added together in a 1:1 intensity ratio. The contribution from the amide deuteron was neglected in both models.

The agreement between the experimental and simulated spectra is good; however, the spectra at the higher temperatures are somewhat narrower than either model predicts. This additional narrowing is likely due to small scale librational motion. The spectra are very sensitive to temperature and therefore to the rate of the molecular motion. An Arrhenius plot was constructed with the rates of the rotation used for the simulations assuming $n = 3$ (Figure 18). The activation energy for the rotation was found to be $14.4 \pm 1 \text{ kJ mol}^{-1}$, which agrees well with the 14.3 kJ mol^{-1} obtained from 3 to 21G/SDD/PBE DFT calculations.

Conclusions

To drive discovery of useful multimetallic clusters with unique catalytic and materials science applications, we must continue to improve methods for their synthesis. In this article we emphasized the propensity for macrocycle **1** to template formation of high nuclearity metal clusters and highlighted a family of heptacadmium metallocavatands. These metallocavatands exhibit a wide variety of interesting dynamic processes ranging from dimerization to ligand exchange to guest exchange. SCXRD and low temperature ^1H NMR spectroscopy revealed the previously assigned $\mu_3\text{-O}$ ligand is actually a $\mu_3\text{-OH}$ ligand and DFT calculations confirmed an energetic preference for the $\mu_3\text{-OH}$ ligand. Although the difference is structurally subtle, the $\mu_3\text{-OH}$ ligand dramatically impacts the host–guest chemistry of these metallocavatands, resulting in a $\mu_3\text{-OH}$ ligand capable of H-bonding to encapsulated guest molecules deep in the cavity. Hydrogen bonding and metal coordination synergy inside metallocavatand capsules results in an exceptionally high packing coefficient, 0.80, for encapsulated DMF. Variable temperature ^1H NMR spectroscopy revealed dimerization to be an entropy driven event that is highly solvent dependent. Formation of two DMF-cadmium coordination bonds inside the monomer's cavity is proposed as the rate-determining step for both dimerization and acetate exchange in DMF- d_7 . 3-fold rotation of an encapsulated DMF molecule was also quantified by variable-temperature solid-state ^2H NMR spectroscopy. Future research efforts will focus on the discovery of new molecular metal clusters and exploring the potential of metallocavatands to simultaneously act as both molecular reaction vessels and multimetallic catalysts.

Acknowledgment. F.L. thanks INSTM for support during his sabbatical leave and the Department of Chemistry at UBC for the

(78) Wann, M.-H.; Harbison, G. S. *J. Chem. Phys.* **1994**, *101*, 231–237.

warm hospitality. D.L.B. thanks the Natural Sciences and Engineering Research Council (NSERC) of Canada and the Ontario government (Early Researcher Award) for funding. M.J.M., A.J.G., and P.D.F. thank NSERC and UBC for funding this research. P.D.F. is grateful to UBC for a graduate fellowship. This paper is dedicated to the memory of Prof. Keith Fagnou at the University of Ottawa.

Supporting Information Available: Synthetic details, full characterization of new compounds, kinetic analysis, crystallography, and additional computational information. This material is available free of charge via the Internet at <http://pubs.acs.org>.

JA910419H